[redacted]

AMERICAN NUCLEONICS CORPORATION
6036 VARIEL AVENUE,
WOODLAND HILLS, CALIFORNIA 91364
PHONE (213) 347-4500

INTERIM FINAL REPORT

A Study of the Electromagnetic Interaction Between Planetary Bodies and the Solar Wind

By Dr. K. Schwartz

March 1971

Prepared under Contract No. NAS2-5876 by
AMERICAN NUCLEONICS CORPORATION
Woodland Hills, California

for

AMES RESEARCH CENTER
NATIONAL AERONAUTICS AND SPACE ADMINISTRATION

TABLE OF CONTENTS

TABLE OF CONTENTS

TABLE OF CONTENTS

1.0 Introduction

The major task carried out under Contract NAS2-5876 was the development of theoretical and computational techniques for calculating the time dependent electromagnetic response of a radially inhomogeneous moon. The importance of this task was two-fold. The techniques were first used to analyze the experimental data from the LSM (Lunar Surface Magnetometer) thus providing the first in-depth diagnostics of the Lunar interior (Sonett et. al., 1971, a and b). The theory was also incorporated into an existing computer code designed to calculate the thermal evolution of planetary bodies. The previous calculations (Sonett et. al., 1969) had relied only on unipolar induction. The new program will provide a tool for examining the effect of heating from the TE mode (poloidal magnetic field) as well as the TM mode (toroidal magnetic field).

The theoretical discussion of the problem of the electromagnetic response of a radially inhomogeneous moon is presented in Section 2. The method of obtaining various potential solutions for the vector wave equation is shown along with the spherical harmonic expansion of these potentials. Formulas are derived for the radial equations which reduce the problem of obtaining the solutions to an initial value calculation.

The theory is applied to the problems of the near surface thermal gradient of the moon, and the overall lunar electrical conductivity in Sections 3 and 4, respectively. By comparing the experimental data with calculated results for lunar models, the thermal gradient is bracketed between 1.5 and 4°K/km near the lunar surface. A computer inversion using the complete experimental spectrum is invoked in Section 4 to obtain the lunar conductivity. This work has been reported in Sonett et. al. (1971, a and b). The major discovery in this work is a prominent peak in the electrical conductivity at a radius of 1500 kilometers. The lunar conductivity exhibits a precipitous fall off on either side of 1500 kilometers.

A new version of the computer code used to generate the data for Sonett et. al. (1969) is described in Section 5. The major change is the inclusion of the time dependent electric fields for the joule heating. The program with all of its subroutines has been checked and is operational from an experimental aspect. Because of the inherent complexity of the overall heating problem, more short computer runs must be laid out and made in order to determine an optimum mode of investigation for this program.

2.0 Electromagnetic Induction in the Moon

2.1 Mechanism

Electromagnetic induction in the Moon is dependent upon the existence of a large class of discontinuities and waves in the solar wind. The forcing function which drives the induction is composed of the steady interplanetary magnetic field upon which is superimposed a hydromagnetic radiation continuum due to (1) plasma waves arising presumably in the solar atmosphere and subsequently convected and propagated outwards, (2) waves due to local instabilities in the solar wind, and (3) discrete large amplitude events such as collision-free shock waves, tangential discontinuities, and Alfvén waves.

The formal statement of the electromagnetic interaction problem rests upon division of the fields into parts which correspond to toroidal and poloidal magnetic fields. These are excited respectively by a) the interplanetary electric field (as perceived in a frame of reference comoving with the Moon) given by $\underline{E}_m = \underline{v} \times \underline{B}$, where $\underline{v}$ is the velocity of the Moon relative to the solar wind and $\underline{B}$ the instantaneous interplanetary magnetic field, and b) the time rate of change of the interplanetary field, $\dot{\underline{B}}$. The two modes correspond respectively to transverse magnetic (TM) and transverse

electric (TE) excitation. Both modes display strong frequency dependence ($f = \omega/2\pi$ where ω is the angular frequency in radian/sec). The magnitude of the TE transfer function goes to unity as frequency, $f \to 0$, and increases with increasing f. The TE mode currents which close wholly in the lunar interior, tend to be concentrated where the waves damp substantially. With increasing frequency, the poloidal magnetic field becomes compressed into shells of decreasing thickness. The exclusion of the field from the interior of the moon, coupled with the confinement of the field at the lunar surface by the solar wind pressure on the sunlit side of the moon produces a magnification of the resultant magnetic field at the lunar surface.

The TM mode attains peak value for $f = 0$; it remains approximately constant with increasing f until a combination of core and lithospheric constitutive parameters forces the currents to pass wholly through the crust whereupon it decreases with further increase of f. This mode is responsible for the steady state bow wave phenomena.

Theoretical treatments of the lunar interaction with the solar wind generally include the effect of the solar wind dynamic pressure in confining the induced field lines (Blank and Sill, 1969; Schubert and Schwartz, 1969).

This is provided in the model by a field confining surface current layer in the solar wind just ahead of the lunar surface. Preliminary examination of the lunar response using the LSM data shows a strong amplification of incident tangential discontinuities whose free stream properties are monitored by Explorer 35 (Sonett et. al.,1971 a and b). The amplification occurs only for the vector components tangential to the surface; the normal component tends to follow the interplanetary value. Thus, the existence of a thin confining current layer appears verified for the sunward side of the Moon. The very strong excitation implies that the lines of force are confined within the Moon to a crustal layer having an electrical conductivity substantially less than that of the deeper layers.

2.2 Theory of the Induction for Harmonic Excitation

A complete treatment of the electromagnetic interaction would require appropriate matching of the interior fields to those in the plasma surrounding the Moon. A less complicated interaction model can be used for the present day moon-solar wind electromagnetic induction problem because the flow field exterior to the sunlit side of the moon shows no marked perturbation from the presence of the Moon aside from the diamagnetic cavity (Colburn et. al., 1967; Ness et. al., 1967). Based on

this lack of a scattered field up stream in the plasma, an analysis for the sunward hemisphere is carried out for an inhomogeneous Moon immersed within a perfectly conducting space. The compressional effect of the solar wind momentum flux is taken into account mathematically by postulating an electrical current layer just above the lunar surface.

Previous discussion of the electromagnetic response of the Moon to solar wind forcing functions have been limited to models of concentric, constant electrical conductivity spherical shells (Blank and Sill, 1969, Schwartz and Schubert 1969, Schubert and Schwartz, 1969, Sill and Blank, 1970). Also, the analyses of Blank and Sill (1969) and Sill and Blank (1970) are valid only for low frequencies. Their work corresponds to the retention of only the first term in the spherical harmonic expansion of the forcing field. Electromagnetic waves of frequency high enough to be confined to the near surface region of constant temperature gradient require for their complete description higher order terms in a spherical harmonic expansion. The theory presented in this section is applicable to a Moon whose electrical conductivity, σ , varies with radial position in an arbitrary manner. In addition, higher order terms in a spherical harmonic expansion of the fields are retained throughout the

theoretical development.*

We consider the interaction of a solar wind forcing field of the form

$$\underline{H} = \hat{\underline{y}}\, H_0 \exp\left\{ i\left(\frac{2\pi z}{\lambda} - \omega t\right)\right\} \qquad (1)$$

$$\underline{E} = \hat{\underline{x}}\, \mu v H_0 \exp\left\{ i\left(\frac{2\pi z}{\lambda} - \omega t\right)\right\} \qquad (2)$$

with a radially inhomogeneous Moon. The cartesian coordinate system (x, y, z) with unit vectors $\hat{\underline{x}}$, $\hat{\underline{y}}$, $\hat{\underline{z}}$, is fixed relative to the Moon and has its origin at the Moon's center. The Moon moves with speed v in the negative z-direction. The quantities H_0 and $\lambda = v/f$ are the amplitude and wavelength, respectively, of the magnetic field oscillation and the circular frequency ω is $2\pi v/\lambda$. The amplitude of the electric field oscillation is $\mu v H_0$, where μ is the permeability of the solar wind. We follow the formalism of Wyatt (1962) who considered the scattering of electromagnetic plane waves from inhomogeneous spherically symmetric objects

*The following theoretical development, as applied to the Moon problem, was first presented by Schubert and Schwartz (1970). This work was then incorporated into the LSM report (Sonett et. al., 1971 a,b).

in connection with the problem of determining the nuclear scattering cross-sections. His work appears to have been based on earlier work of Lahiri and Price (1939).

2.2.1 Formal Solution for $\sigma(r)$

The solutions of Maxwell's equations can be represented as the superposition of two linearly independent fields, the transverse electric ($\underline{E}^m$, $\underline{H}^m$) and the transverse magnetic ($\underline{E}^e$, $\underline{H}^e$) . It can be shown that these two sets of fields are completely determined from two potentials, Ω^m and Ω^e which satisfy the equations

$$\nabla^2\Omega^m + k^2\Omega^m = 0 \tag{3}$$

$$\nabla^2\Omega^e - \frac{1}{k_1 r}\frac{dk_1}{dr}\frac{\partial}{\partial r}(r\Omega^e) + k^2\Omega^e = 0 \tag{4}$$

where

$$k^2 = \omega^2\mu\varepsilon + i\sigma\mu\omega \tag{5}$$

$$k_1 = i\omega\varepsilon - \sigma \tag{6}$$

and μ and ϵ are the magnetic permeability and electrical permittivity of the Moon. Although some possibility exists that local effects are significant in increasing the value of μ over the free space value, there is presently no evidence for this. An upper bound for the global permeability of 1.8 μ_0 is given by Behannon (1968). In the following discussion the values assumed for the global permeability and permittivity of the Moon are the free space values of these quantities. Possible departures of the permittivity from the free space value are insignificant in the subsequent application of this theory.

First, consider the transverse magnetic (TM) or superscript e mode, characterized by the vanishing of the radial component of the magnetic field. The first step in obtaining the potential for this mode is to write out Maxwell's equations using (5) and (6):

$$\nabla \times \underline{E} = k_2 \underline{H} \tag{7}$$

$$\nabla \times \underline{H} = -k_1 \underline{E} \tag{8}$$

where $$k_2 = i\omega\mu \tag{9}$$

$$k^2 = -k_1 k_2 \tag{10}$$

It can easily be seen that the radial component of (7) is satisfied exactly if

$$E_{\varphi}^{e} = \frac{1}{r \sin \theta} \frac{\partial U^{e}}{\partial \varphi} \tag{11}$$

$$E_{\theta}^{e} = \frac{1}{r} \frac{\partial U^{e}}{\partial \theta} \tag{12}$$

where r, θ, φ are the spherical coordinate triplet and U^e is a scalar potential. If (11) and (12) are next inserted into the θ and φ components of (8) the resultant equations are

$$\frac{\partial}{\partial r}\left(rH_{\varphi}^{e}\right) = k_1 \frac{\partial U^{e}}{\partial \theta} \tag{13}$$

$$\frac{\partial}{\partial r}\left(rH_\theta^e\right) = \frac{-k_1}{\sin\theta}\frac{\partial U^e}{\partial \varphi} \tag{14}$$

By defining a potential Ω^e by

$$U^e = \frac{1}{k_1}\frac{\partial}{\partial r}\left(r\Omega^e\right) \tag{15}$$

it can be seen that (13) and (14) are satisfied exactly if

$$H_\theta^e = -\frac{1}{\sin\theta}\frac{\partial \Omega^e}{\partial \varphi} \tag{16}$$

$$H_\varphi^e = \frac{\partial \Omega^e}{\partial \theta} \tag{17}$$

Inserting (15) into (11) and (12) gives

$$E_\theta^e = \frac{1}{k_1 r}\frac{\partial^2}{\partial r \partial \theta}\left(r\Omega^e\right) \tag{18}$$

$$E_{\varphi}^{e} = \frac{1}{k_1 r \sin\theta} \frac{\partial^2}{\partial r \partial \varphi} (r\Omega^e) \tag{19}$$

Finally, one must obtain an equation relating E_r^e to Ω^e and a partial differential equation for Ω^e. From the radial component of (8) together with (16) and (17) one obtains

$$\frac{k_1 E_r^e}{r} = -\nabla^2 \Omega^e + \frac{1}{r^2} \frac{\partial}{\partial r} \left(r^2 \frac{\partial \Omega^e}{\partial r} \right) \tag{20}$$

From either of the two transverse components of (8) together with (16) and (18) or (17) and (18) one obtains

$$\left\{ \frac{\partial}{\partial \varphi} \text{ or } \frac{\partial}{\partial \theta} \right\} \xi = 0 \tag{21}$$

where

$$\xi = \frac{k_1 E_r^e}{r} - k^2 \Omega^e + \frac{1}{k_1 r} \frac{\partial k_1}{\partial r} \frac{\partial}{\partial r} (r\Omega^e) - \frac{1}{r} \frac{\partial^2}{\partial r^2} (r\Omega^e) \tag{22}$$

If separation of variables is assumed, then the only solution for (21) is $\xi = 0$. With this result, equation (20), and after some algebraic manipulation one obtains

$$E_r^e = \frac{1}{k_1}\left\{\frac{\partial^2}{\partial r^2} - \frac{1}{k_1 r}\frac{\partial k_1}{\partial r}\frac{\partial}{\partial r} + k^2\right\}(r\Omega^e) \quad . \tag{23}$$

and the determining partial differential equation for Ω^e :

$$(\nabla^2 + k^2)\Omega^e - \frac{1}{k_1 r}\frac{\partial k_1}{\partial r}\frac{\partial}{\partial r}(r\Omega^e) = 0 \quad . \tag{24}$$

It should be noted that the vanishing of the divergence of $\underline{D}(= \epsilon\underline{E})$ has not been invoked in order to obtain this set of solutions. This restriction was erroneously required in Wyatt's paper. In fact, the divergence equation is used to obtain the charge distribution which is <u>not</u> zero in the TM mode when the conductivity is a function of position.

The complete solution of Maxwell's equation within the sphere requires a second set of solutions,

the transverse electric (TE) or magnetic solutions, denoted by superscript m. In these solutions $E_r^m = 0$. One obtains a set of potentials U^m and Ω^m in a manner completely analogous to the procedure followed above. In this case, however, the roles of (7) and (8) are interchanged. From the radial component of (8) one deduces a potential U^m such that

$$H_\theta^m = \frac{1}{r} \frac{\partial U^m}{\partial \theta} \tag{25}$$

$$H_\varphi^m = \frac{1}{r \sin \theta} \frac{\partial U^m}{\partial \varphi} \tag{26}$$

Then using the transverse components of (7) with equations (25) and (26) one is led to the potential Ω^m such that

$$U^m = \frac{1}{k_2} \frac{\partial}{\partial r}(r\Omega^m) \tag{27}$$

$$E_\varphi^m = - \frac{\partial}{\partial \theta} \Omega^m \tag{28}$$

$$E_\theta^m = \frac{1}{\sin\theta}\frac{\partial \Omega^m}{\partial \varphi} \tag{29}$$

$$H_\theta^m = \frac{1}{k_2 r}\frac{\partial^2}{\partial r \partial \theta}(r\Omega^m) \tag{30}$$

$$H_\varphi^m = \frac{1}{k_2 r \sin\theta}\frac{\partial^2}{\partial r \partial \varphi}(r\Omega^m) \tag{31}$$

Following the same technique as for the electrical potential one obtains for H_r^m :

$$H_r^m = \frac{1}{k_2}\left(\frac{\partial^2}{\partial r^2} + k^2\right)(r\Omega^m) \tag{32}$$

and for the partial differential equation for Ω^m :

$$(\nabla^2 + k^2)\Omega^m = 0 \tag{33}$$

The solution of equations (24) and (33) can now be obtained via separation of variables. The equations for

determining $(\underline{E}^m, \underline{H}^m)$ and $(\underline{E}^e, \underline{H}^e)$ from the potentials of Ω^m and Ω^e are presented compactly in Appendix A.

2.2.2 Spherical Harmonic Solutions in the Moon

The solutions for equations (3) and (4) are easily obtained in terms of spherical harmonics by the method of separation of variables. The boundary conditions, used to fix the arbitrary constants of the solutions, are that the solutions are bounded at $r = 0$ and that the tangential components of the electric field are continuous at the lunar surface. For the transverse electric mode this is equivalent to the continuity of the normal component of the magnetic field $(\underline{B} = \mu\underline{H})$. A discontinuity is permitted in the tangential magnetic field because of the confinement of the induced field by the solar wind pressure. This confinement is accomplished by a current sheet at the moon-plasma interface.

The potentials Ω^m and Ω^e are given by

$$\Omega^m = \mu V H_o \frac{a}{r} \sin \varphi \sum_{\ell=1}^{\infty} \beta_\ell A_\ell^m G_\ell^m(r) P_\ell^1(\cos \theta) \qquad (34)$$

$$\Omega^e = H_o \frac{a}{r} \cos \varphi \sum_{\ell=1}^{\infty} \beta_\ell A_\ell^e G_\ell^e(r) P_\ell^1(\cos \theta) \qquad (35)$$

where (r, θ, φ) are the spherical polar coordinates, a is the lunar radius, $P_\ell^1(\cos\theta)$ are the associated Legendre polynomials and

$$\beta_\ell = \frac{i^\ell(2\ell+1)}{\ell(\ell+1)} , \quad i = \sqrt{-1} \tag{36}$$

The functions G_ℓ^m and G_ℓ^e are solutions of the differential equations

$$\frac{d^2G_\ell^m}{dr^2} + \left\{k^2 - \frac{\ell(\ell+1)}{r^2}\right\} G_\ell^m(r) = 0 \tag{37}$$

$$\frac{d^2G_\ell^e}{dr^2} - \frac{1}{k^2}\frac{dk^2}{dr}\frac{dG_\ell^e}{dr} + \left\{k^2 - \frac{\ell(\ell+1)}{r^2}\right\} G_\ell^e(r) = 0 \tag{38}$$

In Sonett et. al. (197la) the appearance of A_ℓ^e and A_ℓ^m were suppressed, these constants being incorporated into the definitions for G_ℓ^m and G_ℓ^e . The exact form of the boundary condition at $r = a$ is obtained by using the spherical harmonic expansion for the incident and internal fields, given in Appendix B. The boundary conditions for the fields are given by

$$A_\ell^m \, G_\ell^m(a) = j_\ell(2\pi a/\lambda) \tag{39}$$

$$A_\ell^e \left.\frac{dG_\ell^e}{dr}\right|_{r=a} = \frac{k^2\lambda^2}{4\pi^2 a} \frac{d}{da} \left(a j_\ell(2\pi a/\lambda)\right) \tag{40}$$

where $j_\ell(x)$ is the spherical Bessel function of order ℓ .

2.2.3 Behavior of the Solutions G_ℓ^m and G_ℓ^e Near $r = 0$

In the center of the Moon, near $r = 0$, it is reasonable to assume that $\frac{dk}{dr}$ becomes vanishingly small. Then G_ℓ^m and G_ℓ^e in the vicinity of $r = 0$ are of the form

$$\lim_{r\to 0} G_\ell^{m,e}(r) \rightarrow r j_\ell(k_o r) \tag{41}$$

where k_o is the propagation constant at $r = 0$. Therefore, at $r = 0$

$$G_\ell^{m,e}(o) = 0 \tag{42}$$

$$\frac{d}{dr}\left(G_\ell^{m,e}\right)\Big|_{r=0} = 0 \tag{43}$$

For numerical calculations the boundary conditions expressed by (42) and (43) are useless. However, an auxilliary function can be defined which makes the solution of (37) or (38) more amenable to digital computer techniques. Define the function $N_\ell^{m,e}(r)$ by

$$G_\ell^{m,e}(r) = r^{\ell+1} N_\ell^{m,e}(r) \tag{44}$$

Then from (37) and (38) the differential equations for $N_\ell^{m,e}$ are

$$\frac{d^2}{dr^2} N_\ell^m + \frac{2(\ell+1)}{r} \frac{dN_\ell^m}{dr} + k^2 N_\ell^m(r) = 0 \tag{45}$$

$$\frac{d^2 N_\ell^e}{dr^2} + \left\{ \frac{2(\ell+1)}{r} - \frac{d}{dr}(\ln k^2) \right\} \frac{dN_\ell^e}{dr} + \left\{ k^2 - \frac{1}{r}\frac{d}{dr}(\ln k^2) \right\} N_\ell^e(r) = 0 \tag{46}$$

and by using (41) the boundary conditions at $r = 0$ become

$$N_\ell^{m,e}(o) = \frac{2^\ell \ell! k_o^\ell}{(2\ell+1)!} \tag{47}$$

$$\frac{d}{dr} N_\ell^{m,e}\Big|_{r=0} = 0 \tag{48}$$

The constant in (47) can also be absorbed in $A_\ell^{m,e}$ to give as an alternate condition to (47),

$$N_\ell^{m,e}(o) = 1 \tag{47a}$$

The boundary conditions at $r = a$ then become

$$A_\ell^m = j_\ell(2\pi a/\lambda) \Big/ \left[a^{\ell+1} N_\ell^m(a) \right] \tag{49}$$

$$A_\ell^e = \frac{\left(k^2\lambda^2/4\pi^2 a\right)\frac{d}{da}\left(a j_\ell(2\pi a/\lambda)\right)}{\frac{d}{dr}\left\{r^{\ell+1} N_\ell^e(r)\right\}\Big|_{r=a}} \qquad (50)$$

For those cases where the differential equation (either (45) or (46)) can be integrated over the entire range $0 \le r \le a$ the use of the auxiliary functions provides a means for reducing the problem to the solution of an initial value computation. Care must be taken, however, because of the nature of the differential equation. These equations are basically diffusion equations, the solutions becoming exponentially damped as r decreases from a toward zero. For higher frequencies and, hence, smaller local skin depths $\delta = \sqrt{\frac{2}{\omega\mu\sigma}}$, the attenuation may become so great that significance will be lost in the integration scheme. For these cases an alternative procedure would be to integrate the original differential equation ((37) or (38)) from some depth b where the local skin depths δ is small ($\delta \le (a-b)$), and assume that the fields vanish for $r < b$. The equations can then be solved as a boundary value problem with $N_\ell^{e,m}(b) = 0$ and $N_\ell^{e,m}(a)$ determined through equations (49) and (50).

3.0 The Near Surface Lunar Thermal Gradient

3.1 Introduction

The initial results from the Apollo 12 lunar surface magnetometer experiment show that on the sunward hemisphere the moon displays a magnetic field response to the interplanetary electromagnetic field which is larger by one-half order of magnitude than an equivalent vacuum bounded case. This strong interaction provides the basic justification for the current layer at the moon-plasma interface, which is used in the theoretical development in Section 2. Without this layer there can be no signal increase over the vacuum case. The field increase or amplification is dependent on the combined exclusion of the induced field by a highly conducting lunar core and the confinement at the sunward surface of this same field by the solar wind pressure.

The interior field exclusion is related to the damping of the TE wave as it propagates into the moon. For a constant conductivity moon the damping occurs at progressively shallower depths as the frequency increases. This phenomenon is accentuated when the electrical conductivity increases with depth. Even for an inverted conductivity profile one can easily be convinced that the magnetic field compression at the lunar surface increases with increasing frequency.

The first LSM data points for the magnetic field magnification were obtained for frequencies at the high end of the usable band for the Explorer 35 Ames magnetometer and LSM combination, .02 to .04 Hertz. These frequencies are high enough to lead to the expectation that the electromagnetic damping in the lunar crust will occur at some depth d where the lunar temperature profile can be described by a linear thermal gradient approximation; i.e.,

$$T(r) = T_s + T_r(a-r) \quad , \quad b < r < a \qquad (51)$$

where b is the smallest radius for the approximation and where T_s is the surface temperature in degrees Kelvin, a is the lunar radius (1740 kilometers), T_r is the thermal gradient in °K/km and r is the radial distance in kilometers. The estimates of the thermal gradient are dependent on the model conductivity assumed although there are obvious constraints provided by the range of validity of the linear gradient approximation and necessary high internal temperatures for the low conductivity models.

Since only the electrical conductivity σ occurs in the differential equations for the field (equations 37 and 38) rather than $T(r)$ the model dependence is obvious. As a final point, one should note that

the magnetic field exclusion occurs at depths where the local skin depth, $\delta = \sqrt{2/\omega\mu\sigma}$, is of the order of one kilometer and the quantity $(\sigma/\omega\epsilon)$ is much greater than unity. Hence, the equations (37) and (38) are basically diffusion equations and the value of ϵ is of no consequence to the resultant field distribution. By combining equation (51) with various models for rock electrical conductivity and then comparing the resultant calculated magnetic field with the experimental data, a series of estimates can be obtained for the lunar thermal gradient near the surface.

3.2 Theory

The refined data from the LSM experiment is generally present as a ratio of the field measured at the LSM to the inducing field measured at Explorer 35. This data is further obtained only after Fourier decomposition of both original signals. Thus, the experimental data provides a transfer function of the moon to electromagnetic induction. In order to make a comparison between the theoretical and experimental data, a theoretical transfer function must be defined. This is easily accomplished for the TE mode by going to Appendices A and B of Section 2 and equation (34). First, remember that the boundary condition for the TE mode requires that the radial components of the magnetic field be continuous.

Then the transfer function must relate the tangential components of the field. A normalized harmonic transfer function is defined for the TE mode by

$$T_{\ell}^{m}(r) = \frac{\frac{d}{dr} G_{\ell}^{m}(r)}{\frac{1}{a}\frac{d}{da}(aj_{\ell}(2\pi a/\lambda))} \qquad (52)$$

This provides the ratio, for each harmonic, of the TE mode magnetic field anywhere in the moon to the inducing magnetic field in that same harmonic at the lunar surface. This definition for a transfer function which is independent of θ and φ cannot be made for the TM mode magnetic fields. Instead, the induced TM magnetic fields can only be compared to the inducing TE magnetic fields. The difficulty that arises can be seen by examining the limiting case as the frequency goes to zero. For this limit the magnetic field components of the driving field for the TM mode vanish while the induced TM components can have any value (theoretically) depending on the electrical conductivity of the moon model. This would lead to extremely large values of a transfer function even though both the driving field and induced field are well behaved. As an alternative, the TM transfer function has been defined as

$$T_\ell^e(r) = \frac{2\pi i a^2}{\lambda r} \frac{G_\ell^e(r)}{\frac{d}{da}(a j_\ell(2\pi a/\lambda))} \tag{53}$$

For the models used in this section, the T_ℓ^e values are too small to be of importance.

3.3 Conductivity Models

The electrical conductivity of rocky material is conventionally represented by a function of the form

$$\sigma = \sum_{i=1}^{3} \sigma_{0i} \exp(-\frac{\epsilon_i}{kT}) \tag{54}$$

where σ_{0i} is the mobility (conductivity for $T = \infty$), ϵ_i is an activation energy, the energy required to raise an electron from a valance band into a conduction band, $\overline{k}$ is Boltzmann's constant, and T the absolute temperature. The dependence of conductivity upon temperature and activation energy as expressed by equation (54) follows the classical theory of semiconductors, but information so far developed in geology lags the former significantly. Nevertheless, from an experimental standpoint, equation (54) does represent conduction sufficiently well so that application to the present problem can be made. The total conduction is made up of an impurity

range, one in which intrinsic electronic conduction dominates and lastly an upper temperature range in which ionic conduction takes over. The latter is likely not significant in the application of this paper and is disregarded. The use of a conductivity function at atmospheric pressure extrapolated to depth can have the effect of reducing the apparent conductivity because of the presence of interstitial cracks. We have no information on this for lunar samples. Any error would be in the direction of increasing the calculated thermal gradient so that this must be regarded as a limitation, as is the paucity of samples and the generalization to bedrock.

We consider here two conductivity functions thought to represent extremes for the lunar material. For an Apollo 11 lunar crystalline rock (sample 10024-22), Nagata et. al., (1970) found

$$\epsilon_1/\overline{k} = 5800\,^{\circ}K \quad , \qquad \epsilon_2/\overline{k} = 14{,}500\,^{\circ}K \quad ,$$

$\sigma_{01} = 7.9$ mhos/m and $\sigma_{02} = 3.7 \times 10^{6}$ mhos/m . It has been found that an Apollo 12 rock (sample 12053-47) has a more complicated dependence of conductivity upon temperature but displays a generally similar behavior to

that of the Apollo 11 sample with somewhat reduced conductivity over the range measured.

There is good reason to suspect that these samples are not representative of the basement rock. For example, they could not constitute the basic rock of the Moon for the basalt transforms to eclogite at 12 kb pressure, and the density of this polymorph is too high to match the overall lunar density. Other more subtle geochemical arguments having to do, for example, with the incompatible element concentration in the basalts, suggest that the interior is better represented by a periodtite containing a substantial fraction of olivine. For this reason we have chosen as the other end point calculation an olivine conductivity function (England et. al., 1968) for which $\epsilon_1/\overline{k} = 10{,}670\,^{\circ}K$, $\epsilon_2/\overline{k} = 31{,}300\,^{\circ}K$, $\sigma_{01} = 55$ mhos/m and $\sigma_{02} = 4\times10^{7}$ mhos/m . The behavior of the Moon rock and olivine as functions of temperature are illustrated in Figure 1.

3.4 Numerical Calculations

For sufficiently small skin depths it is unnecessary to integrate the equations of the previous section to the center of the Moon. It is sufficient to replace the deep interior of the Moon by a perfectly conducting sphere and integrate the equations from the lunar surface to the surface of the perfectly conducting core.

The exact location of this lower boundary is unimportant as long as the local skin depth is small. For convenience in the numerical computations to follow, the lower boundary has been set at a depth of 250 km. The transfer function was obtained for several values of the frequency, f , and a solar wind speed of 400 km/sec.

The equations derived in Section 2 have been numerically integrated for the lunar thermal gradient Moon models described above. For all models T_s was taken as -30°C or 243°K. The behavior of the real and imaginary parts of the transfer function for the $\ell = 1$ TE mode (equation (52)) is shown in Figure 2 for the Nagata-Moon rock conductivity, for a frequency of .04 Hz and thermal gradients of 2, 3 and 4°K per kilometer. Except for the lowest thermal gradient, the magnetic fields and, hence, the transfer function are well damped below r = 1500 kilometers.

Extensive calculations for the TE mode, $\ell = 1$, transfer function have been made for the two conductivity functions. The data from these calculations is shown in Tables 1 and 2 where the magnitude and phase of the transfer functions are given for frequencies of .02, .03 and .04 hertz and for thermal gradients from 1°K to 7°K per kilometer for the England-olivine conductivity. Data was calculated only up to 4°K/km for the Nagata-Moon rock

T_r (°K/km)	Freq (Hertz)		
	.02	.03	.04
1	2.4/-9.5°	2.6/-9.8°	2.9/-10°
2	3.9/-9°	4.4/-9.2°	4.7/-9.7°
3	5.3/-8.3°	6.1/-8.6°	6.4/-9.0°
4	6.7/-8.0°	7.5/-8.3°	8.1/-8.4°

TABLE 1

TE Mode $\ell = 1$ transfer function calculated using the Nagata-lunar basalt conductivity

T_r (°K/km)	Freq (Hertz)		
	.02	.03	.04
1	1.5/-6.1°	1.6/-6.2°	1.7/-6.2°
2	2.4/-7.8°	2.6/-7.7°	2.8/-7.7°
3	3.3/-8.3°	3.6/-8.2°	3.9/-8.2°
4	4.1/-8.5°	4.5/-8.5°	4.8/-8.5°
5	4.9/-8.8°	5.3/-8.7°	5.7/-8.6°
6	5.7/-8.9°	6.2/-8.8°	6.6/-8.7°
7	6.4/-9.0°	7.0/-8.9°	7.4/-8.9°

TABLE 2

TE Mode, $\ell = 1$, transfer function calculated using the England-olivine conductivity

because of its much higher conductivity and resultant large transfer functions T_1^m . The amplitude data of Tables 1 and 2 are displayed graphically in Figure 3. From this figure it is clear that for a given value of T_1^m at a given frequency the olivine conductivity requires a higher thermal gradient and, hence, a higher internal temperature. Calculations were also carried out for higher order harmonics for the TE mode. These results listed in Table 3 were obtained for $f = .04$ Hertz, a solar wind velocity V of 4×10^5 m/s and a lunar radius of 1.74×10^6 meters. For these values the argument of the Bessel functions in the driving term ($2\pi fa/v = 2\pi a/\lambda$) is approximately unity. It can be seen that the amplitude of the transfer functions and, hence, the amplification of the field decreases with increasing harmonics. In addition, for this set of parameters, the higher order harmonics in the forcing functions are of decreasing importance in the harmonic expansion of the forcing field at the lunar surface. These forcing functions are in the ratio $1.0:0.18:0.025:2.8 \times 10^{-3}:2.5 \times 10^{-4}$. Only the second harmonic produces any appreciable correction in the field. The magnitude of this correction will decrease with decreasing frequency since for

$$\lim_{x \to o} j_n(x) \rightarrow \frac{(2x)^n \, n!}{(2n+1)!}$$

Nagata Moon Rock (Basalt)

Harmonic	Thermal Gradient		
	2	3	4
1	4.7/-9.7°	6.4/-9°	8.1/-8.4°
2	3.0/-9.6°	4.1/-8.9°	5.1/-8.3°
3	2.2/-9°	3.0/-8.5°	3.8/-8.2°
4	1.8/-8.4°	2.5/-8.2°	3.0/-7.9°
5	1.6/-7.6°	2.1/-7.7°	2.6/-7.6°

England-Olivine

Harmonic	Thermal Gradient			
	4	5	6	7
1	4.8/-8.5°	5.7/-8.6°	6.6/-8.7°	7.4/-8.9°
2	3.0/-8.5°	3.3/-8.5°	4.2/-8.6°	4.7/-8.7°
3	2.3/-7.9°	2.7/-8°	3.1/-8.3°	3.5/-8.4°
4	1.9/-7.4°	2.2/-7.6°	2.5/-8°	2.8/-8.2°
5	1.6/-6.8°	1.9/-7.1°	2.1/-7.6°	2.4/-8°

TABLE 3

Normalized Surface Tangential Transfer functions for $f = .04$ Hertz, $v = 4 \times 10^5$ m/s, $a = 1.74 \times 10^6$ meters. In the harmonic expansion the forcing functions for the harmonic are in the ratio $1:0.18:0.025:2.8 \times 10^{-3}:2.5 \times 10^{-4}$.

3.5 Discussion

The response functions shown in Figure 2 have the general form one would expect for magnetic induction in a layered spherical conductor for which the inner conductivity is much greater than the conductivity near the surface. The phase change with increasing depth is a characteristic of the change of the governing differential equation from one which is essentially a Laplace equation to a diffusion equation. The strong damping of the induced field starts in the region of the phase change. It is clear that the field penetration decreases as the thermal gradient increases. The property that the induction is relatively constant in the outermost regions corresponds to the fact that in this region both the real current $\underline{J} = \sigma\underline{E}$ and the displacement current $\epsilon\partial\underline{E}/\partial t$ are negligible. The results of the calculation are qualitatively similar to results which would be obtained for a two layer calculation. For instance, if the Moon had infinite conductivity for $r < b$ and zero conductivity for $b < r < a$, the transfer function $T^m(r)$ for those frequencies where $\left|2\pi a/\lambda\right| << 1$ is given by

$$T^m(r) = \frac{1 + 1/2\,(b/r)^3}{1 - (b/a)^3} \qquad b < r < a \qquad (55)$$

From this equation it is obvious that if b is close to a , $T^m(r)$ is very nearly constant and equal to $1.5/(1 - (b/a)^3)$.

The magnitude of the transfer functions given in Tables 1 and 2 and shown in Figures 2 and 3 are indicative of the compression of the induced magnetic field between the solar wind at the lunar surface and the highly conducting lunar interior. For a given conductivity function and frequency the field amplification increasing with increasing thermal gradient. Similarly, for fixed thermal gradient and conductivity the magnification increases with frequency.

The penetration of the magnetic field into the Moon increases as the frequency decreases for a fixed thermal gradient and conductivity function or as the thermal gradient decreases for a fixed frequency and conductivity function. The decrease in the magnetic field amplification corresponds to the increase in penetration. Since the true thermal gradients must be expected to decrease with increasing depth, the lower frequency waves will penetrate even further into the Moon than is indicated by the constant gradient analysis. This analysis is only meaningful for the highest frequencies where the major damping occurs within the first 200 to 300 kilometers. The depth of penetration has been obtained for

some selected cases which are shown in Table 4. The depth shown in this table corresponds to the position of the first zero of the real part of the transfer function.

Thermal Gradient	Nagata Moon-Basalt .04 Hertz	.02 Hertz
2°K/km	249 km	266
3	178	189
4	140	148
	England-Olivine	
4	247	264
5	207	222
6	186	192
7	159	170

TABLE 4

Depth of penetration of the induced field using the first zero of the real part of the TE , $\ell = 1$ transfer function

It can be seen from this table and from Tables 1 and 2 that similar values of the damping depth give approximately the same value for the transfer function.

3.6 Comparison with Experimental Data

The presently accepted experimental values for $\left|T_1^m\ (a)\right|$ are shown in Figure 5 with the error bars (Sonett et al. 1971a and 1971b). The experimental values for .02, .03 and .04 Hertz are shown in the curves in Figure 3 with appropriate error bars. An immediate difficulty arises because the value of T_1^m for .02 Hertz is greater than for the other two frequencies. There is, as yet, no theoretical explanation for this. However, using the data for .03 and .04 Hertz a lower limit can be obtained for the thermal gradient of 1.4°K/km. This is obtained for the Negata-basalt. If one uses a less conducting material such as the olivine, a higher value of the thermal gradient is obtained, 2.7°K/km.

It has been suggested that some TM mode admixture may be occurring. To investigate this possibility the TM mode $\ell = 1$ transfer function was calculated for a frequency of .03 Hertz and thermal gradient of 4°K/km using the Moon basalt conductivity. A value of $2.5 \times 10^{-4}\ \underline{/0°}$ was obtained for the transfer function showing that the low conductivity of the crust was cutting off the

excitation of this mode within the Moon. To the conductivity equation given by (54) with the basalt values a constant conductivity was added; i.e.,

$$\sigma(T) = \sigma_{Basalt}\ (T) + \sigma_o \qquad (56)$$

The results of these calculations are shown in Table 5.

TABLE 5

TM transfer functions for f = .03 Hertz, T_r = 4°K/km and Nagata Basalt

σ_o	T^e
0	$2.5 \times 10^{-4} \angle 0°$
10^{-8}	$7.7 \times 10^{-3} \angle 0°$
10^{-7}	$.072 \angle -.17°$
10^{-6}	$.56 \angle -1.25°$

It can be seen that the TM mode will not produce any measurable effect unless the surface conductivity is at

least of the order of 10^{-6} mhos/meter. This corresponds to a temperature of 365°K for the Moon basalt and 590°K for the olivine, much higher than the mean surface lunar temperature of 243°K.

4.0 The Conductivity of the Moon

4.1 Introduction

In the previous section an attempt was made to bracket the near surface lunar thermal gradient. In this section the total spectral data obtained from the LSM experiment is used to provide an estimate for the conductivity of the moon from approximately r = 400 km to the surface. The general properties of both the LSM and Ames magnetometer on Explorer 35 have been given (Dyal and Parkin, 1971, Milhalov et. al, 1968). The theory has been described in Sections 2.0 and 3.0. This work is also included in Sonett et. al. (1971b).

4.2 Experimental Data

The spectral determination and coordinate transformations for the experimental data were carried out at Ames Research Center (Sonett et. al. 1971b). The forcing field defined by Explorer 35 measurements is transformed into the local LSM coordinate system (x is along the normal outwards from the surface, y is easterly and z is northerly at the site of ALSEP and the LSM). Power spectral densities are obtained for the magnetic field time series at both Explorer 35 and LSM for all three components.

A representative set of spectra at both Explorer and LSM for the y and z magnetic field components (tangent to the surface) is shown in Figure 4. The forcing spectra are seen to display the expected f^{-2} dependence characteristic

of interplanetary fluctuations, while the LSM shows an f^{-1} dependence. Thus, significant frequency dependent power amplification is apparent in the record. A combination of all the data points $\bar{A}(f) = \left\{\frac{1}{2}\left(A_y^2(f) + A_z^2(f)\right)\right\}^{\frac{1}{2}}$ for all frequencies up to 0.040 Hz has been made. See Figure 5.

4.3 Lunar Electrical Conductivity Profile

The theory of lunar induction, discussed earlier, has been used to derive a profile of electrical conductivity from the empirical transfer function.(1) The theoretical amplification for the lowest TE mode, computed by numerically integrating equation (45) with a radially dependent conductivity, is matched to the empirical transfer function using a Newton-Raphson iterative scheme. This scheme readjusts the entire conductivity profile to yield amplifications which best fit the data in a least-squares sense over the entire frequency range. This has been carried out using frequency values of 0.83, 1.75, 5, 12, 17, 22, 25, and 35 millihz. The conductivity profile is characterized by its values at the radial locations r = 800, 1200, 1400, 1450, 1490, 1510, 1550 and 1740 km. For r <800 km the conductivity σ is set to the value at r = 800 km; elsewhere a linear interpolation of log σ is used.

(1) This theory, and the computer program for deriving the conductivity profile from the empirical transfer function were developed by American Nucleonics Corp.

The computer calculation is started with a continuous conductivity profile defined by 8 parameters, as described above. Numerical integrations are carried out to obtain values of amplification at the eight frequencies. A comparison of these amplifications with the data provides the Newton-Raphson scheme with the input required to adjust the 8 conductivity parameters to yield a profile whose corresponding theoretical amplification curve is a better least-squares fit to the empirical transfer function. The iteration is continued until an adequate fit is obtained. The result of such a fit to the empirical amplification curve $\overline{A} = \left\{\frac{1}{2}\ (A_y^2 + A_z^2)\right\}^{\frac{1}{2}}$ is shown in Figure 5. The differences between the theoretical amplification and the empirical $\overline{A}$ are very likely attributable to the various complications of the excitation process not accounted for by the theory, as well as considerations of computer running time which limits the number of frequencies and conductivity parameters (spatial resolution) employed.

A conductivity profile is associated with the theoretical amplification curve of Figure 5 and is shown in Figure 6. The conductivity profiles derived from the iterative least squares inversion for A_y , A_z and their on standard deviation limits (see Sonett et. al., 1971, a or b). The prominent spike is an invariant characteristic

of the inversion for each set of data. It is centered at about $r = 1500$ km where the conductivity is nearly 10^{-2} mhos/m. The inner minimum lies at about $r = 1400$ km and the conductivity appears to rise at greater depth. Gross bounds on the conductivity profile are seen in the insert; these are determined from the one standard deviation limits of the various A's, but do not themselves represent one standard deviation limits on the conductivity profile.

The computer calculations for Figures 5 and 6 started with a constant conductivity of 10^{-4} mhos/m . However, a number of computations have been carried out using different values for uniform starting conductivities (e.g., 10^{-3} and 10^{-5} mhos/m) and different radial locations. In every case tested, initial convergence was rapid and the final conductivity profile invariably displayed the prominent spike near $r = 1500$ km . For the profiles reported here, several values of r were chosen in the neighborhood of $r = 1500$ km to better define the conductivity spike.

Whereas the large spike in conductivity is a persistent feature of the inversions, the character of the conductivity profile at greater depth, where the conductivity appears to rise, is not so certain and our results for the conductivity at these depths must remain

tentative. The surface amplification is a rather insensitive function of core conductivity because of the relatively small core volume and the distance to the surface.

4.4 Comparison with Other Conductivity Profiles

A physical understanding of the appearance of the large conductivity spike can be obtained as follows. In a two layer model with an infinitely conducting core and a non-conducting shell the amplification of the tangential magnetic field components' equation (55), can be written in the form

$$T = 1 + \frac{3}{2} \frac{(\text{Core volume})}{(\text{Shell volume})}$$

This simple result requires that the high frequency skin depth barrier be near r = 1500 km for an amplification ≈ 4 . At frequencies above 0.02 Hz essentially no wave penetration takes place through this barrier. Thus, the volume available in the core for field lines is insignificant compared to that in the non-conducting shell. This means that the amplification becomes independent of frequency; i.e., $dA/df \to 0$ at high frequency. Concurrent with the high frequency limitation is the requirement that A drop to near unity at the lower frequencies. If it were assumed that the electrical conductivity were monotonic, so that the interior conductivity were uniformly

high, then the low frequency amplification would be in excess of the observed values.

The inadequacies of monotonic conductivity profiles are shown in Figure 7. The experimental r.m.s. amplification data $\overline{A}$ (circled points with associated error bars) can be compared with the amplification curve for the $\overline{A}$ conductivity profile of Figure 6 (labelled "best fit") and amplification curves of several monotonic conductivity profiles. The "2 layer" amplification curve was calculated for a model with a core of radius of 1560 km and a constant conductivity of 7.6×10^{-4} mhos/m, and a shell of zero conductivity. This value of the core conductivity provides a best fit to the experimental $\overline{A}$ for the given core radius. Other best fit two layer models with different core radii have been investigated; the one used in Figure 7 yields an amplification curve which matches the data most closely. The amplification curve labelled DYAL and PARKIN (1971) was computed from a 3 layer conductivity model proposed by these authors. The parameters of their model are $\sigma = 10^{-2}$ mhos/m for $0 < r < 1044$ km, $\sigma = 1.7 \times 10^{-4}$ mhos/m for $1044 \text{ km} < r < 1653$ km and $\sigma = 0$ in the outer shell. In other 3 layer conductivity models consistent with the data analysis of DYAL and PARKIN (1971), the outer boundary of the region of intermediate conductivity can be located

anywhere between $r = 1653$ and 1740 km . We have computed the amplification curves for a number of these additional 3 layer models; none provide a better fit to the observational curve. Also shown in Figure 7 are amplification curves from conductivity profiles proposed by SILL (1971) (model 3 in that paper) and NESS (1969). Other conductivity models investigated by SILL (1971) fit the experimental data no better than his model 3. The conductivity model of NESS (1969) consists of a core of radius 1426 km with $\sigma = 8 \times 10^{-5}$ mhos/m , and a non-conducting shell. Amplification curves from conductivity models of WARD (1969) were also considered but these were rejected upon comparison with the observational data.

The "2 layer" amplification curve shown in Figure 7 is, compared to the experimental data, high at $f < 0.0035$ Hz and $f > 0.03$ Hz , and low in the range 0.01 Hz $< f < 0.02$ Hz . The data show a flat response at frequencies above 0.02 Hz, whereas the slope of the "2 layer" curve is high at these frequencies. Furthermore, as the frequency increases the curvature of the data changes from positive to negative at about 0.003 Hz. The "2 layer" amplification curve is everywhere concave up. This "s" shaped character of the experimental data is faithfully reproduced only by our "best fit" conductivity profile. Further work is in progress to improve

the high frequency slope of our "best fit" model. This will probably lead both to a higher value of the maximum conductivity and a steeper slope of the conductivity profile at the outer edge, effects which will tend to sharpen the conductivity spike in order to allow penetration of low frequency magnetic field fluctuations.

4.5 Compositional and Thermal Model

The electrical conductivity profile cannot be explained by a uniform material and a plausible thermal profile. In the region from the surface to $r = 1500$ km where the conductivity attains its maximum value, the rise of conductivity with depth is a reasonable consequence of the accompanying increase of temperature in a material of uniform composition. Below $R = 1400$ km the apparent rise in conductivity is again explainable by an increase in temperature. On the other hand, the precipitous decrease of electrical conductivity by 2 to 3 orders between $r = 1500$ and 1400 km cannot be explained as due to temperature. Either a compositional change, phase change, or a combination of the two is required. Thus, a reasonable model for stratification of the Moon, limited by the present poor spatial resolution of the analysis indicates a core out to $r \approx 1400$ km overlain by a mantle of higher conductivity material, plus possibly a transition layer at $r = 1400 - 1500$ km .

In order to infer a temperature profile from the conductivity profile it is necessary to use conductivity-temperature functions of known rock materials. The Apollo basalts (Schwerer et. al., 1970; Nagata et. al., 1970) are representative of the most conducting rock matter known. On the other hand, olivine (dunite) or olivine-peridotite (England et. al., 1968) is representative of poorly conducting geological material. The peak conductivity value found in the lunar mantle corresponds to a temperature of about 450°C for lunar basalt or 950°C for olivine. Since the temperature just under the lunar surface is -30°C, the corresponding thermal gradients in the outer mantle are about 2°K/km and 4°K/km. These estimates correspond to those obtained in Section 3.0 for .02 Hertz.

5.0 Early Planetary Heating by Electromagnetic Induction

5.1 Introduction

Sonett et. al. (1968) and Sonett et. al. (1970) have given convincing argument for the possibility of a short, intense heating episode caused by electromagnetic induction, this episode occurring during the initial formative years of the planetary body. In these two papers the electrical heat source was the unipolar induction field which is the d.c. limit of the TM mode discussed in Section 2.0. The model parameters have been thoroughly presented in the two references and in Schwartz (1969). An obvious deficiency of the theory, as presented to date, is the reliance on only the d.c. field component to the exclusion of the rest of the frequency spectrum. To remedy this situation, the original planetary heating computer program has been rewritten to provide a method for evaluating the separate and combined contributions to the planetary heating from the TM and TE modes as a function of frequency. The program is still in the check-out stage as far as practical results are concerned. The individual subroutines have all been checked out but the actual modes of operation have not been worked out. Some brief runs have been made to ensure that all the routines work properly together.

5.2 The Driving Field

As described in Sonett et. al. (1970) it is assumed that the sun passed through a T Tauri stage 4.5 billion years ago on the way to becoming a main sequence star. During T Tauri the sun maintained both a high spin rate, near the centrifugal limit, and a high surface magnetic field. The driving field for the electromagnetic induction is assumed to be the quasi steady state rotating sector structure of the magnetic field and the frozen-in $\underline{V} \times \underline{B}$ electrical field which is convected past the planet by the solar wind. A two level sector structure for the magnetic field is assumed so that the magnetic field $\underline{H}$ and also the electric field $\underline{E} = \underline{V} \times \mu\underline{H}$ have magnitude H_o and E_o, respectively, but change sign (direction) every half period of the solar rotation. If the solar period is 2τ ($\tau = \pi/\omega_o$ where ω_o is the local time solar spin rate) then the time dependence of driving fields is given by

$$\begin{pmatrix} E \\ H \end{pmatrix} = \begin{pmatrix} E_o \\ H_o \end{pmatrix} \begin{cases} +1 & 2n\tau \le t \le (2n+1)\tau \\ -1 & (2n+1)\tau \le t \le 2(n+1)\tau \end{cases} \qquad (57)$$

The average power deposited by joule heating can be obtained using Fourier Series techniques with the result that for any given mode (i.e., TE or TM)

$$\overset{\circ}{H}(r) = \sigma(r) \sum_{n=-\infty}^{+\infty} \left| C_n \bar{V}_n(r) \right|^2 \tag{58}$$

where $\overset{\circ}{H}(r)$ is the power density in watts/m^3, $\sigma(r)$ is the electric conductivity in mhos/meter, $V_n(r)$ is the normalized electric field in volts/meter and C_n is the Fourier coefficient for the driving term

$$C_n = \begin{pmatrix} E_o \\ H_o \end{pmatrix} \begin{cases} 0 & n \text{ even} \\ \frac{-2i}{n\pi} & n \text{ odd} \end{cases} \tag{59}$$

The square of the total input electric field is

$$\left| E \right|^2 = E_o^2 \frac{8}{\pi^2} \sum_{m=o}^{\infty} (2m+1)^{-2} = E_o^2 \tag{60}$$

Thus, the total driving field looks, in magnitude, identical to the driving field for a constant field of E_o . In fact, the total input for the TM portion of the driving field is equivalent to the input for the unipolar induction where one assumes $C_o = 1$ and $C_n = 0$ for $n = 0$.

The highest solar spin rate, at $t = 0$ years, is $(\omega_o)_{max} = 4.2 \times 10^{-4}$ radians/sec or $(f_c)_{max} = 6.67 \times 10^{-5}$ Hertz . If one sums the magnitude from the first 10 terms of the TM mode, the omitted terms constitute 2% of the total used.

5.3 General Program Concept

The main program, called HEAT03, solves the basic problem of the thermal history of a planetary body. Input data is read into the program in the main body and through a subroutine CONIN. Provision is made for radio nuclide heat sources in the subroutine set RADIO and AHEAT. The electromagnetic heat sources are obtained through the subroutine ERAD and a subsidiary subroutine FSET. The subroutine ERAD sets up the T Tauri flow parameters, the driving electromagnetic field, solar spin rate and the electrical conductivity. The calculations of the electric fields and the joule heating are carried out through FSET. In the present version of the code, the calculation can be made for:

(1) the d.c. unipolar generator

(2) the TE mode for a series of n frequencies ($n \geq 1$) where $f_n = (2n-1)f_o$ where f_o is the solar spin rate

(3) the TM mode for the same series of n frequencies as (2).

Combinations of (1) and (2) or (2) and (3) can also be obtained. For the present n is set equal to 1 in FSET because more investigation is needed to determine an optimum method for running the program. The program is designed for no melting and therefore no radioactive concentration. The radioactive sources are assumed to be uniformly distributed within the body. The electrical heating term has two parts, one from the tangential electric field and one from the radial electric field (TM mode only). The program can be set through input data to use either or both parts.

5.4 Input Deck

The following is the make up of a typical run. Each card set is explained.

Card 1 This is a descriptive header card using columns 2 through 80. It must be used but can be blank.

Card 2 Name List M1. There are three inputs on this name list.

ATIM is the start time of the calculation in years.

TTESTZ is a skip time in years. For TTESTZ = $\delta > 0$ the electric field joule heating will not be calculated any more often than δ years, except when a printout of the thermal profile and the heat sources is called for.

EFCT determines which components of the electric field will be used for the joule heating.

1. E_r , σE_r^2
2. $E_{Tangential}$, σE_τ^2
3. $\sigma(E_r^2 + E_\tau^2)$

Card Set 3 Name List M2. This name list has 15 inputs.

GTC This is the time constant, γ, for the solar magnetic field in units of $eons^{-1}$ (1 eon = 10^9 years). The maximum permissible value is .457. For any larger value the sun becomes centrifugally unstable at time zero according to the despin theory used for the program. The magnetic field

has the variation

$$B(t) = B_{4.5} \exp \gamma(4.5-t)$$

RBAR This is a parameter which might just as well be an internal constant, equal to r_s^2/r_{se} where $r_s = 6.99765 \times 10^8$ meters solar radius. $r_{se} = 1.495 \times 10^{11}$ meters - earths distance from sun. RBAR = 3.2754×10^6 meters.

RG This is the distance between the sun and the planetary body under investigation, measured in astronomical units (a.u.). For the earth, RG = 1.

DP This is a constant term which is added to the electrical conductivity in ERAD. DP can have any value (in mhos/meter) but for the most recent calculations, DP = 0.

ENZ This is the particle flux density of the solar wind at 1 a.u. and at t = 4.5 eons. The present value is taken as 10^7 protons per cubic meter.

ENTTZ This is the particle flux density for a T Tauri flow at 1 a.u., $t = 0$, and normalized to a solar mass loss $\Delta M = M_{\odot} = 2 \times 10^{30}$ kilograms. For the assumed velocity and time decay, ENTTZ = 8.6×10^{14} protons per cubic meter.

GSW Time constant for the solar wind flux density, taken as 1.0214 per eon.

GTT Time constant for the T Tauri flux density, taken as 1200 per eon.

VTZ T Tauri flow velocity at $t = 0$: 2×10^{5} meter/sec.

VELZ Solar wind flow velocity at $t =$ 4.5 eons; 4×10^{5} meters/sec.

GVZ Solar wind velocity time constant; 85.5/eon.

TS Average space temperature at T = 4.5 eons - normal, 273° Kelvin.

TTS Increment in space temperature caused by T Tauri obscuration; $0 \leq TTS \leq 500°$.

GTTS Time constant for decay of obscuration: 1.2×10^{-6} per year.

Card Set 4 Name List M3 has six entries.

DELA Spatial difference step for inner portion of the planetary body in the solution of the thermal diffusion equation, normally 2×10^6 meters .

DELB Spatial difference step for the outer layer of the planetary body in the solution of the thermal diffusion equation. For early heating with T Tauri flow 1×10^5 meters is used. For late times or when T Tauri is not important 5, 10 or 20 $\times 10^5$ meters can be used.

FINR Fraction of a solar mass being lost during the T Tauri stage: $0 \leq$ FINR. We have been using FINR = .5.

PELT First estimate for a time step (in years) in the solution of the thermal diffusion equation. PELT must be greater than 0 , preferably 10^3 years for T Tauri heating, 10^6 years for heating by radionuclides only.

MSTEP Total number of points in the spatial grid for the solution of the thermal diffusion equation. It cannot exceed 200. With DELA = 2×10^6 meters and DELD = 10^5 meters MSTEP = 183 and IMSTP = 83 for the moon.

IMSTP Number of space points using DELA. If r_i is the radial distance from the center of the planetary body to the i^{th} point then

$$r_i = \begin{cases} (i-1)\text{DELA} \; ; & 1 \leq I \leq \text{IMSTP} \\ (\text{IMSTP}-1)\text{DELA} + (i-\text{IMSTP})\text{DELB}; & \\ \text{IMSTP} \leq \text{MSTEP} & \end{cases}$$

Card Set 5 Name List M4, four entries.

XI = 0 , XI is the normalized start point for the integration of the electric field equation.

INIT = 2
NSAV = 0 } These two parameters set up the integration scheme as an initial value problem. For cases where the internal conductivity of the planet becomes too large, INIT is switched to zero automatically. NSAV is an

internal program parameter which must be zero initially but takes on the value one for program switching. If INIT becomes zero, XI is stepped to a value greater than 0 , and the field equations are solved as a boundary value problem. This is a time consuming method and should be avoided if at all possible.

IFCT This parameter determines which joule heating method will be used.

1. Unipolar generator (DC limit of TM mode)
2. TE mode
3. TE mode and unipolar generator
4. TM mode
5. TE mode and TM mode

The following data cards are called from the auxilliary subroutine CONIN:

Card Set 6 Name List C1.

NT This is the number of times at which thermal profile and output data will be printed out. $1 \leq NT \leq 50$.

The time points TB must be set up so that TIB(I+1) > TIB(I) .

TIB — Time points for output, in years.

Card Set 7 Name List C2.

NTØ — Number of points for the starting temperature, TØ(I) in °C as a function of position RØ(I) in kilometer. $2 \leq NT\emptyset \leq 50$.

RØ(I) — Position at which the temperature is.

TØ(I) — The data from TØ is interpolated to cover the points for the thermal integration in the main program using the subroutine TINTR.

NSORC — This is the number of radio nuclide heat sources $1 \leq NSORC \leq 8$.

The next card set, set 8, numbering from one to eight, depending on NSORL, gives the radio nuclides for the planetary heating. The cards are in a 3 x, 3A4, 3E15.5 format. The 3A4 portion of the format reads in the radio nuclide name.

TEXT(I) — Radio nuclide name (= 1,2,3).

W(I) — Radio nuclide abundance, grams/gram.

B(I) Radio nuclide heat generation, joules/gram-year.

FLAM(I) Radio nuclide decay constant, per year.

Card Set 9 Name List CØN.

DENS The planetary density in grams/cc (assumed uniform in this program).

FN Index of refraction used in thermal conduction formula: FN = 1.7.

E Energy gap in e.v. for the portion of the radiation opacity derived from the electronic conduction term: E = 3 electron volts.

CP Heat capacity: 1.2 Joules/gram-degree.

FKF Not used in program: = Ø

EØ The opacity (=100/cm).

SIGØ Supposed electrical conductivity at infinite temperature (=10 mhos/cm).

C Lattice thermal conductivity (=7.889 x 10^5 Joule/cm-year-°K).

Card Set 10 Name List C3.

Al(I) I = 1, 6. These coefficients are for the electrical conductivity $\sigma(T)$ in mhos/meter, where T is the temperature. The conductivity is given by

$$\sigma(T) = \sum_{i=1}^{3} Al(2i-1)\exp\left\{-Al(2i)/T\right\}$$

In ERAD the conductivity becomes

$$\sigma_T(T(r)) = \sigma(T) + DP$$

where $\sigma(T)$ is shown above and DP is the additive constant in read in name list M2.

5.5 Test Cases

A limited number of test cases were run with the new computer program. In each case the electrical conductivity function used was Olivine (Rikitake 1966) with

$$\sigma(T) = 0.1e^{-5800/T} + 10.e^{-19000/T} + 3.5 \times 10^4 e^{-35000/T}$$

Further, only a uniform temperature moon model was used with $T = 500°C = 773°K$ giving a constant lunar conductivity of 5.4×10^{-5} mhos/meter .

First, consider the TM mode and the unipolar generator. For the unipolar generator the joule heating during the T Tauri phase was 8.7×10^{-3} joules/gram-year each from both the radial and tangential electric fields. There was a K factor of .37 and a power ratio of 2.4 (see Sonett et. al.,1970 for complete explanations of these terms). For the TM mode test case only the $n = 1$ harmonic was used. The resultant heating was 7.4×10^{-3} joules/gram-year with a k factor of .36 and a power ratio of 2.5. The contributions from the higher harmonic decreases as $(2n+1)^{-2}$. The ratio of the TM heating to unipolar heating is $(8/\pi^2)$ if one takes into account the slight difference in the k factors. Note that the heating input in this case is four orders greater than the radio nuclide heating for a chondritic source, 1.28×10^{-6} joules/gram-year (Fricker and Reynolds, 1967).

The contribution from the TE mode is somewhat more difficult to analyze. The electric field for the TE mode is proportional to the frequency for the low frequencies of interests. Figure 8 shows the TE heat input for the first harmonic and the sum of the first 125 non zero harmonics. Note that the sum term is

approximately 100 times greater than the single harmonic. This occurs because the amplitude of each harmonic electric field is proportional to $(2n+1)\omega_o$ where ω_o is the solar spin rate and the exciting field decreases as $(2n+1)^{-1}$. Thus, except for the affect of attenuation with depth, each harmonic produces the same electric heating input. The contributions begin to drop off significantly for frequencies greater than 0.1 Hertz ($2\pi a/\lambda \gtrsim 1$).

5.6 Summary

Only the preliminary portion of the investigation of planetary heating by time dependent electromagnetic induction has been completed. The major tool for the investigation is essentially complete, the computer program. Because of the complexity of the program and the problem of planetary heating, great care must be taken in laying out a plan for examining the possible effects of electromagnetic induction on planetary evolution. So far, only a constant temperature case has been investigated for the TE mode. This case produced an inverted heat source with up to ten times greater energy disposition than chondritic nuclides toward the planetary surface. More conducting moon models would have sharpened the slope. Further, in the light of this small data sample, it would appear that the TE mode can not be used for the rapid heating near time zero. The TM mode heating can deposit

10^3 to 10^4 more energy. However, the TM mode heating is critically dependent on the state of the planetary surface electrical conductivity, whereas the TE mode should be unaffected by the surface. Therefore, more initial time models must be examined before one embarks on a long calculation scheme.

6.0 Summary of Report

6.1 Electromagnetic Induction in the Moon

The major effort for the past year, upon which all the other work was based, was the formulation of the theory of electromagnetic scattering by a radially inhomogeneous moon. This formulation was a synthesis of techniques described by Wyatt (1962) and also used originally by Lahiri and Price (1939) and many others. The formalism was combined with the lunar boundary condition first proposed by Blank and Sill (1969) for a two layer moon model. The major advance obtained during this program was generalization to models where the lunar electrical conductivity is an arbitrary function of the radius. Discontinuities can also be handled within this framework. A spherical harmonic expansion was carried out for this theory and harmonics higher than the first are retained. The resultant radial wave function has been transformed in order to produce a mathematical problem which is more tractable for computation; i.e., an initial value problem. For special cases, as in the near surface thermal gradient calculations of Section 3, the solutions were obtained on the computer by a two point boundary value calculation which requires much longer running time.

6.2 Near Surface Thermal Gradient

The initial application of the formalism of Section 2 was the calculation of the TE transfer function for various moon models which could be characterized by a constant thermal gradient near the surface. The compositional models were derived from a lunar basalt (Nagata et. al., 1970) and an olivine (England et. al., 1968). The former constitutes one of the most highly conducting rock materials while the latter is, for low temperature, one of the least conducting rocks. To obtain solutions of the differential equations of Section 2, an iterative technique was carried out to solve a boundary value problem. At some inner point, the field was assumed zero and the slope of the radial term was varied in order to match the surface boundary condition. In combination with the initial LSM data (Sonett et. al., 1971 a and b) these calculations bracket the thermal gradient between 1.4 and 4°K/km. These results were based only on the high frequency response, .02 to .04 Hz.

6.3 Whole Body Lunar Conductivity

By using the entire experimental spectrum from LSM an iterative fit was obtained for the lunar electrical conductivity. The figure of merit for this fit was the sum of the squares of the deviation of the calculated

transfer function from the experimental transfer function. For an eight frequency fit, this value was .06 after five iterations. Much more work remains to be done on this problem to improve the spatial resolution of the conductivity profile. However, a major discovery is the apparent presence of a high peak in the electrical conductivity in the vicinity of $r = 1500$ kilometers in the moon.

6.4 Primordial Planetary Joule Heating

The mathematical results of Section 2 have been incorporated into a computer program for calculating the thermal evolution of planetary bodies. The thermal sources now include the effects of both the TE mode and TM mode. All of the pertinent subroutines have been checked for errors and one set of test runs has been made for each type of joule heating individually. These initial results indicate that the TE mode contribution may be significantly greater than the proposed chondritic radionuclide sources over the outer lunar shell. Further investigation is required, however, to determine the effects of different thermal and conductivity models on this form of heating. The major advantage of TE heating is its insensitivity to a low (or zero) conductivity surface layer.

Appendix A

The fields $(\underline{E}^m, \underline{H}^m)$ and $(\underline{E}^e, \underline{H}^e)$ are related to the potentials Ω^m , Ω^e according to

$$E_r = E_r^e = \frac{1}{k_1}\left(\frac{\partial^2}{\partial r^2} - \frac{1}{k_1}\frac{dk_1}{dr}\frac{\partial}{\partial r} + k^2\right)(r\Omega^e) = \frac{1}{k_1}\frac{\ell(\ell+1)}{r^2}(r\Omega^e) \quad ,$$

$$E_\theta = E_\theta^e + E_\theta^m \; M \; \frac{1}{k_1 r}\frac{\partial}{\partial r}\left(r\frac{\partial \Omega^e}{\partial \theta}\right) + \frac{1}{\sin\theta}\frac{\partial \Omega^m}{\partial \varphi} \quad ,$$

$$E_\varphi = E_\varphi^e + E_\varphi^m = \frac{1}{k_1 r \sin\theta}\frac{\partial}{\partial r}\left(r\frac{\partial \Omega^e}{\partial \varphi}\right) - \frac{\partial \Omega^m}{\partial \theta} \quad ,$$

$$H_r = H_r^m = -\frac{k_1}{k^2}\left(\frac{\partial^2}{\partial r^2} + k^2\right)(r\Omega^m) \quad ,$$

$$H_\theta = H_\theta^e + H_\theta^m = -\frac{1}{\sin\theta}\frac{\partial \Omega^e}{\partial \varphi} - \frac{k_1}{k^2 r}\frac{\partial}{\partial r}\left(r\frac{\partial \Omega^m}{\partial \theta}\right) \quad ,$$

$$H_\varphi = H_\varphi^e + H_\varphi^m = \frac{\partial \Omega^e}{\partial \theta} - \frac{k_1}{k^2 r \sin\theta}\frac{\partial}{\partial r}\left(r\frac{\partial \Omega^m}{\partial \varphi}\right) \quad .$$

Appendix B

The spherical harmonic expansions for the potential and the electromagnetic fields of the transverse electric part of the solar wind excitation are

$$\Omega^m = \mu V H_o \sin\varphi \sum_{\ell=1}^{\infty} \beta_\ell j_\ell\left(\frac{2\pi r}{\lambda}\right) P_\ell^1(\cos\theta)$$

$$\begin{Bmatrix} H_\theta^m \\ H_\varphi^m \end{Bmatrix} = \frac{H_o \lambda}{2\pi i r} \begin{Bmatrix} \sin\varphi \\ \cos\varphi \end{Bmatrix} \sum_{\ell=1}^{\infty} \beta_\ell \frac{d}{dr}\left[r j_\ell\left(\frac{2\pi r}{\lambda}\right)\right] \begin{Bmatrix} \frac{dP_\ell^1(\cos\theta)}{d\theta} \\ P_\ell^1(\cos\theta)/\sin\theta \end{Bmatrix}$$

$$H_r^m = \frac{H_o \lambda}{2\pi i r} \sin\varphi \sum_{\ell=1}^{\infty} \beta_\ell \ell(\ell+1) j_\ell\left(\frac{2\pi r}{\lambda}\right) P_\ell^1(\cos\theta)$$

$$\begin{Bmatrix} E_\theta^m \\ E_\varphi^m \end{Bmatrix} = \mu V H_o \begin{Bmatrix} \cos\varphi \\ -\sin\varphi \end{Bmatrix} \sum_{\ell=1}^{\infty} \beta_\ell j_\ell\left(\frac{2\pi r}{\lambda}\right) \begin{Bmatrix} P_\ell^1(\cos\theta)/\sin\theta \\ \frac{dP_\ell^1(\cos\theta)}{d\theta} \end{Bmatrix}$$

where $$\beta_\ell = \frac{i^\ell (2\ell+1)}{\ell(\ell+1)}, \quad i = \sqrt{-1}$$

The electromagnetic fields and potential for the transverse electric mode in the lunar interior are

$$\Omega^m = \mu V H_o \frac{a}{r} \sin \varphi \sum_{\ell=1}^{\infty} \beta_\ell A_\ell^m G_\ell^m(r) \; P_\ell^1(\cos \theta)$$

$$\begin{Bmatrix} H_\theta^m \\ H_\varphi^m \end{Bmatrix} = \frac{H_o \lambda a}{2\pi i r} \begin{Bmatrix} \sin \varphi \\ \cos \varphi \end{Bmatrix} \sum_{\ell=1}^{\infty} A_\ell^m \beta_\ell \frac{dG_\ell^m}{dr} \begin{Bmatrix} \dfrac{dP_\ell^1(\cos \theta)}{d\theta} \\ P_\ell^1(\cos \theta)/\sin \theta \end{Bmatrix}$$

$$H_r^m = \frac{H_o \lambda a}{2\pi i r} \sin \varphi \sum_{\ell=1}^{\infty} A_\ell^m \beta_\ell \ell(\ell+1) \left(\frac{G_\ell^m}{r} \right) P_\ell^1(\cos \theta)$$

$$\begin{Bmatrix} E_\theta^m \\ E_\ell^m \end{Bmatrix} = \mu V H_o \frac{a}{r} \begin{Bmatrix} \cos \varphi \\ -\sin \varphi \end{Bmatrix} \sum_{\ell=1}^{\infty} A_\ell^m \beta_\ell G_\ell^m(r) \begin{Bmatrix} P_\ell^1(\cos \theta)/\sin \theta \\ \dfrac{dP_\ell^1(\cos \theta)}{d\theta} \end{Bmatrix}$$

The corresponding formulae for the transverse magnetic mode driving field are

$$\begin{Bmatrix} H_\theta^e \\ H_\varphi^e \end{Bmatrix} = H_o \begin{Bmatrix} \sin \varphi \\ \cos \varphi \end{Bmatrix} \sum_{\ell=1}^{\infty} \beta_\ell j_\ell\left(\frac{2\pi r}{\lambda}\right) \begin{Bmatrix} P_\ell^1(\cos \theta)/\sin \theta \\ \dfrac{dP_\ell^1(\cos \theta)}{d\theta} \end{Bmatrix}$$

$$\begin{Bmatrix} E_\theta^e \\ E_\ell^e \end{Bmatrix} = \frac{\mu V H_o \lambda}{2\pi r} \begin{Bmatrix} \cos \varphi \\ -\sin \varphi \end{Bmatrix} \sum_{\ell=1}^{\infty} \beta_\ell \frac{d}{dr}\left[r j_\ell\left(\frac{2\pi r}{\lambda}\right)\right] \begin{Bmatrix} \dfrac{dP_\ell^1(\cos \theta)}{d\theta} \\ P_\ell^1(\cos \theta)/\sin \theta \end{Bmatrix}$$

$$E_r^e = \frac{\mu V H_o \lambda}{2\pi i r} \cos\varphi \sum_{\ell=1}^{\infty} \beta_\ell \ell(\ell+1) j_\ell(2\pi r/\lambda) P_\ell^1(\cos\theta)$$

For the interior fields we have

$$\begin{Bmatrix} H_\theta^e \\ H_\varphi^e \end{Bmatrix} = \frac{H_o a}{r} \begin{Bmatrix} \sin\varphi \\ \cos\varphi \end{Bmatrix} \sum_{\ell=1}^{\infty} \beta_\ell G_\ell^e(r) A_\ell^e \begin{Bmatrix} P_\ell^1(\cos\theta)/\sin\theta \\ \dfrac{dP_\ell^1(\cos\theta)}{d\theta} \end{Bmatrix}$$

$$\begin{Bmatrix} E_\theta^e \\ E_\varphi^e \end{Bmatrix} = \mu V H_o \frac{2\pi i a}{\lambda r k^2} \begin{Bmatrix} -\cos\varphi \\ \sin\varphi \end{Bmatrix} \sum_{\ell=1}^{\infty} \beta_\ell A_\ell^e \frac{dG_\ell^e(r)}{dr} \begin{Bmatrix} \dfrac{dP_\ell^1(\cos\theta)}{d\theta} \\ P_\ell^1(\cos\theta)/\sin\theta \end{Bmatrix}$$

$$E_r^e = -\mu V H_o \frac{2\pi i a}{\lambda k^2 r^2} \cos\varphi \sum_{\ell=1}^{\infty} \beta_\ell \ell(\ell+1) A_\ell^e G_\ell^e(r) P_\ell^1(\cos\theta)$$

REFERENCES

1. Behannon, K. W. (1968), "Intrinsic Magnetic Properties of the Lunar Body", J. Geophys. Res. 73, 7257.

2. Blank, J. L. and W. R. Sill (1969), "Response of the Moon to the Time-Varying Interplanetary Magnetic Field", J. Geophys. Res. 74, 736-743.

3. Colburn, D. S., R. G. Currie, J. D. Mihalov and C. P. Sonett (1967), "Diamagnetic Solar Wind Cavity Discovered Behind the Moon", Science 158, 1040.

4. Dyal, P. and C. W. Parkin (1971), "Electrical Conductivity and Temperature of the Lunar Interior From Magnetic Transient-Response Measurements", submitted to Proc. Apollo 12 Lunar Science Conf., Geochim, Cosmochim. Acta.

5. England, A. W., G. Simmons and D. Strangway (1968), "Electrical Conductivity of the Moon", J. Geophys. Res. 73, 3219-3226.

6. Fricker, P. E., R. T. Reynolds and A. L. Summers (1967), "On the Thermal History of the Moon", J. Geophys. Res. 72, 2649.

7. Lahiri, B. N. and A. T. Price (1939), "Electromagnetic Induction in Non-Uniform Conductors, and the Determination of the Conductivity of the Earth From Terrestrial Magnetic Variations", Phil. Trans. R. Soc. A237, 509-540.

8. Mihalov, J. D., D. S. Colburn, R. G. Currie and C. P. Sonett (1968), "Configuration and Reconnection of the Geomagnetic Tail", J. Geophys. Res. 73, 943-959.

9. Nagata, T., T. Rikitake and M. Kono (1970), "Electrical Conductivity and the Age of the Moon." Presented at the Thirteenth Plenary Meeting, COSPAR, Leningrad, USSR.

10. Ness, N. F., K. W. Behannon, C. S. Scearce and S. C. Cantarano (1967), "Early Results From the Magnetic Field Experiment on Lunar Explorer 35", J. Geophys. Res. 72, 5769.

11. Ness, N. F. (1969), "The Electrical Conductivity and Internal Temperature of the Moon", Goddard Space Flight Center Report X-616-69-191 (also presented as paper K11 at XIIth COSPAR, Prague, May, 1969).

12. Rikitake, T. (1966), "Electromagnetism and the Earth's Interior", Elsevier Press.

13. Schubert, G. and K. Schwartz (1969), "A Theory for the Interpretation of Lunar Surface Magnetometer Data", The Moon 1, 106-117.

14. Schubert, G. and K. Schwartz (1970), "Apollo 12 LSM Experiment: Induction as a Function of the Near Surface Thermal Gradient", AGU Conference, San Francisco, December, 1970, 26.

15. Schwartz, K. and G. Schubert (1969), "Time-Dependent Lunar Electric and Magnetic Fields Induced by a Spatially Varying Interplanetary Magnetic Field", J. Geophys. Res. 74, 4777.

16. Schwartz, K. (1969), "A Study of the Effect of the Electromagnetic Interaction Between the Moon and the Solar Wind", NASA CR 73433.

17. Schwerer, F. C., T. Nagata and R. M. Fisher (1971), "Electrical Conductivity of Lunar Rock and Chondritic Meteorites", submitted to The Moon.

18. Sill, W. R. and J. L. Blank (1970), "Method for Estimating the Electrical Conductivity of the Lunar Interior", J. Geophys. Res 75, 201.

19. Sill, W. R. (1971), "Electrical Conductivity and Temperature of the Lunar Interior", J. Geophys. Res. 76, 251-256.

20. Sonett, C. P., D. S. Colburn and K. Schwartz (1968), "Electrical Heating of Meteorite Parent Bodies and Planets by Dynamo Induction From a Pre-Main Sequence T Tauri Solar Wind", Nature 219, 924.

21. Sonett, C. P., D. S. Colburn, K. Schwartz and K. Keil (1970), "The Melting of Asteroidal-Sized Bodies by Unipolar Dynamo Induction From a Primordial T Tauri Sun", Astrophysics and Space Sci. 7, 446-488.

22. Sonett, C. P., B. F. Smith, D. S. Colburn, G. Schubert and K. Schwartz (1971a), "The Lunar Electrical Conductivity Profile: Mantle-Core Stratification, Near Surface Thermal Gradient, Heat Flux and Composition", Nature, in press.

23. Sonett, C. P., G. Schubert, B. F. Smith, K. Schwartz and D. S. Colburn (1971b), "Lunar Electrical Conductivity From Apollo 12 Magnetometer Measurements: Compositional and Thermal Inferences", Proc. Apollo 12 Lunar Science Conf., Geochim. Cosmochim. Acta, in press.

24. Ward, S. H. (1969), "Gross Estimates of the Conductivity, Dielectric Constant, and Magnetic Permeability Distributions in the Moon", Radio Science 4, 117-137.

25. Wyatt, P. J. (1962), "Scattering of Electromagnetic Plane Waves From Inhomogeneous Spherically Symmetric Objects", Phys. Rev. 127, 5, 1837-1843.

FIGURE CAPTIONS

1. The electrical conductivity of two representative minerals vs. temperatures; a moon basalt after Nagata et. al. (1970) and olivine after England et. al. (1968). The former corresponds to a highly conductive rock while the latter corresponds to a low conductivity rock.

2. Behavior of the real and imaginary parts of the TE transfer function as a function of radius in the moon. This data was obtained using the basalt conductivity (Nagata et. al., 1970) $\sigma = 7.9\ e^{-.5/kT} + 5.1 \times 10^{6}\ e^{-1.25/kT}$. The temperature was assumed to follow the equation $T(r) = 243°K + \dot{T}(a-r)$ with $a = 1740$ km. Thermal gradient $\dot{T}$ of 2, 3 and 4 °K/km were used. The frequency is .04 Hertz.

3. The TE mode transfer function for the basalt and olivine conductivity calculated as a function of the thermal gradient for frequencies of .02, .03 and .04 Hertz. The LSM

$$\overline{A} = \left\{ \frac{A_y^2 + A_3^2}{2} \right\}^{\frac{1}{2}}$$

is also shown.

4. Power spectral density determination for simultaneous magnetic field observations on the lunar surface (Apollo 12) and in the solar wind near the Moon (Explorer 35) (prepared by NASA/ARC). The y component is east and the z component north at the Apollo 12 site. Significant amplification is observed, increasing with frequency. Length of the time series is 2 hours, $\delta = 10^{-5}$ gauss.

5. The rms tangential lunar transfer function, $\bar{A} = [0.5\ (A_y^2 + A_z^2)]^{1/2}$ and the normal transfer function A_x as a function of frequency. The x direction is normal to the lunar surface. The solid line is the value of amplification calculated from the conductivity profile whose corresponding amplification is fitted to experimental values at frequencies of 0.83, 1.7, 5, 12, 17, 22, 25, and 35 millihz.

6. Lunar bulk electrical conductivity profiles determined from the individual transfer functions A_y , A_z , and $\bar{A}$. The prominent rise of σ from the surface inwards to r = 1500 km is apparent for all three cases as well as the subsequent decrease inwards to r = 1400 km followed by a more gradual rise. A tentative version of a lunar thermal profile is shown as the grey overlay with temperatures indicated on the right hand margin. This profile is a fit of conductivities to a Nagata basalt in the mantle, an England olivine in the core, and the known subsurface temperature of -30°C. The insert is shown to suggest extreme values of the σ's using the one standard deviation limits of the A's to calculate conductivities (see Sonett et. al. 1971 a and b).

7. The experimental r.m.s. tangential lunar transfer function, $\bar{A}$, as a function of frequency. The error bars are the same as those in Figures 2 and 4. The curve labeled "best fit" are the values of the amplification for the conductivity profile labelled $\bar{A}$ in Figure 5. The "2 layer" curve was calculated for a model with a core of radius 1560 km and a constant conductivity of 7.6×10^{-4} mhos/m, and a shell of zero conductivity. This value of the core conductivity

provides a best fit to $\bar{A}$ for the given core radius. The Dyal and Parkin (1971) amplification curve was calculated for a model with an inner core of radius 1044 km and a conductivity of 10^{-2} mhos/meter, a middle layer extending to 1653 km with a conductivity of 1.7×10^{-4} mhos/m and an outer layer of zero conductivity. Other amplification curves are based on conductivity models proposed by Ness (1969) and Sill (1971). Note that the "2 layer" curve does not duplicate the "S" nature of the experimental data.

8. T Tauri electrical (joule) heating from the TE mode for a 500°C Rikitake-olivine Moon. The $\sum_{TE}$ curve represents the contribution from the first 125 harmonic terms. The TE_1 curve is the contribution from the first harmonic. The horizontal line at 1.25×10^{-6} joules/gram-year is for a uniform chrondritic radionuclide source after Fricker et. al. (1967).

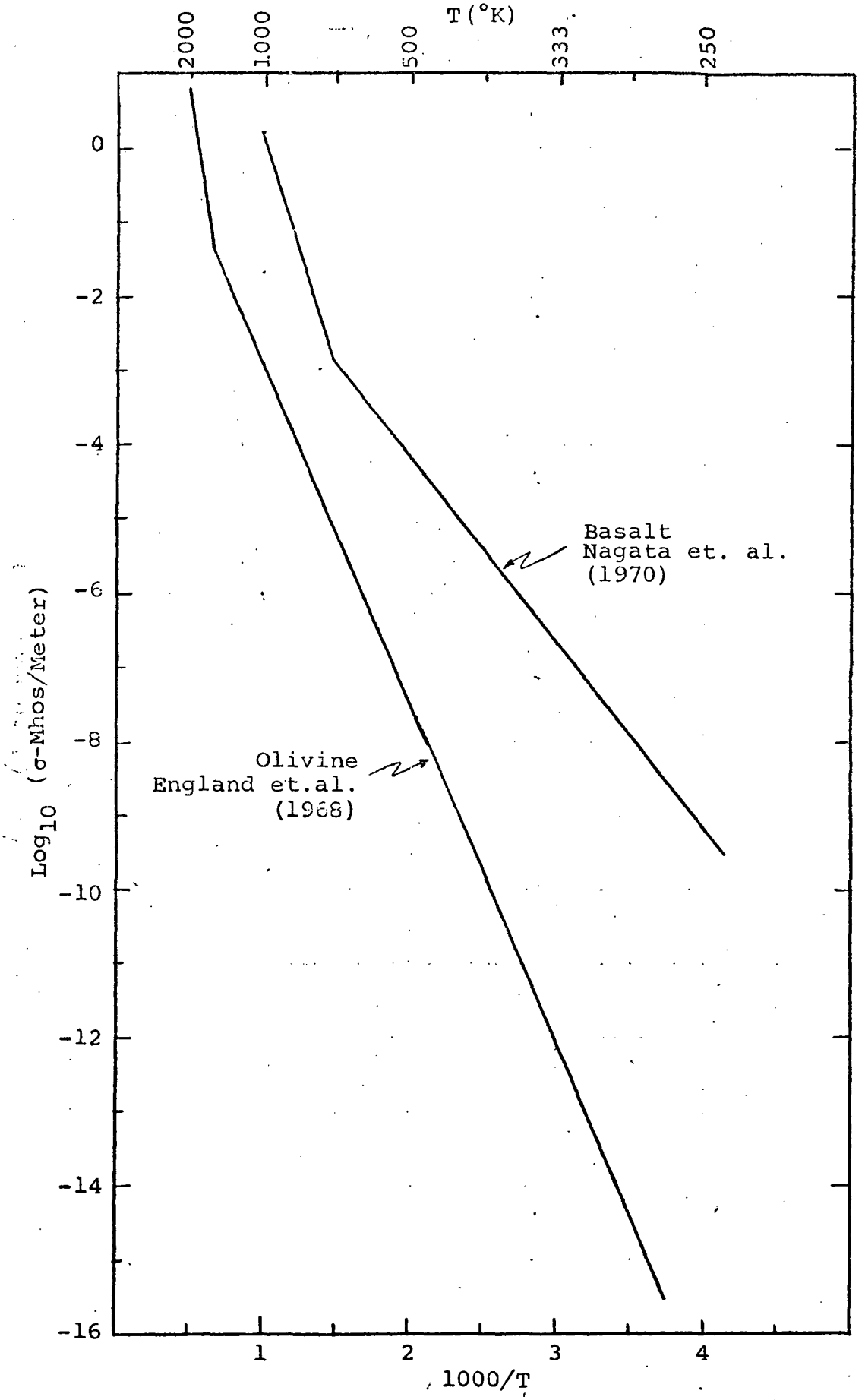
T (°K)
2000
1000
500
333
250
0
-2
-4
-6
-8
-10
-12
-14
-16
Log10 (σ-Mhos/Meter)
Basalt
Nagata et. al.
(1970)
Olivine
England et.al.
(1968)
1
2
3
4
1000/T

FIGURE 1

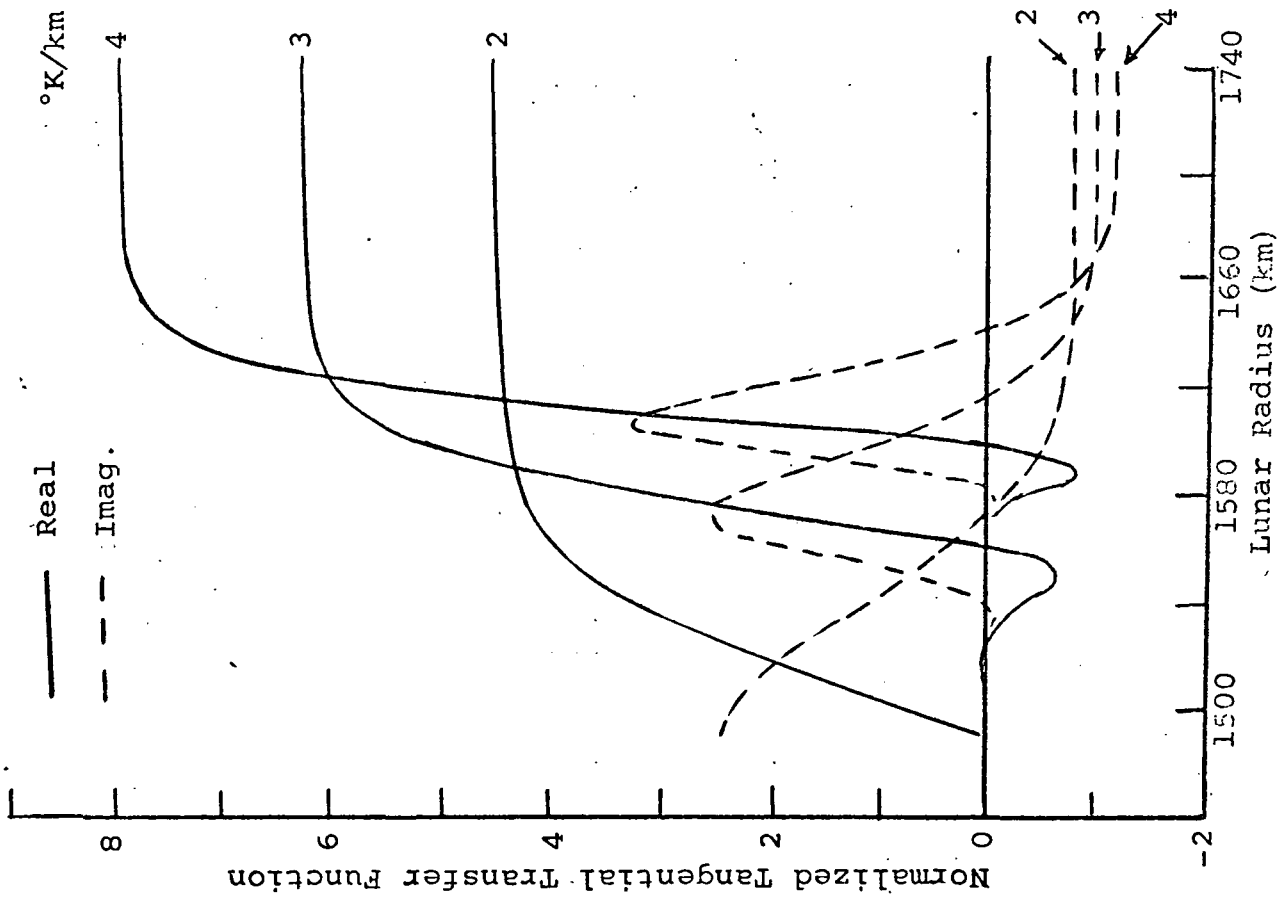
°K/km
4
3
2
Real
Imag.
2
3
4
Normalized Tangential Transfer Function
8
6
4
2
0
-2
1500
1580
1660
1740
Lunar Radius (km)

FIGURE 2

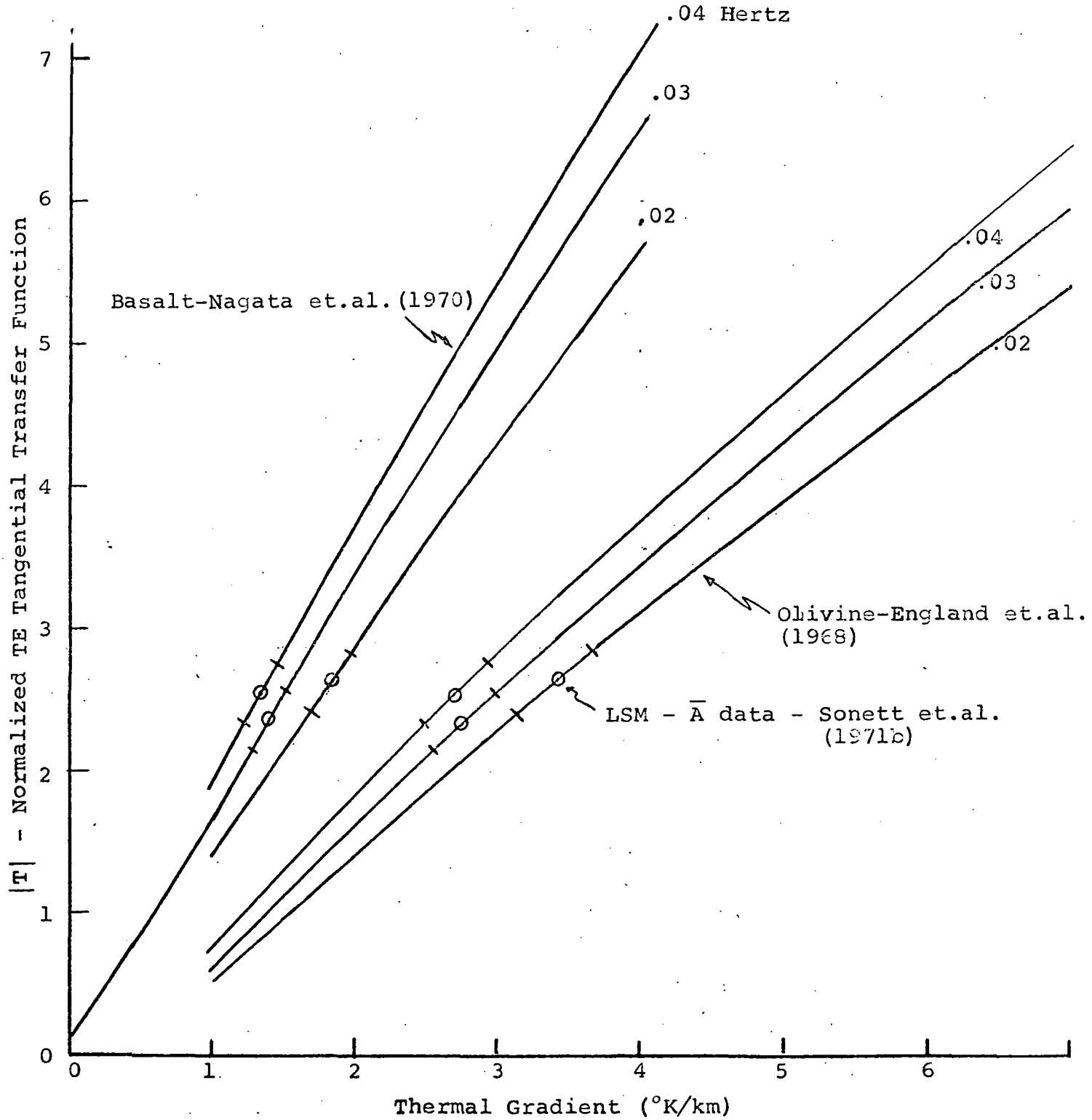
.04 Hertz
.03
.02
Basalt-Nagata et.al. (1970)
.04
.03
.02
Olivine-England et.al. (1968)
LSM - $\bar{A}$ data - Sonett et.al. (1971b)
|T| - Normalized TE Tangential Transfer Function
Thermal Gradient (°K/km)
0
1
2
3
4
5
6
7

FIGURE 3

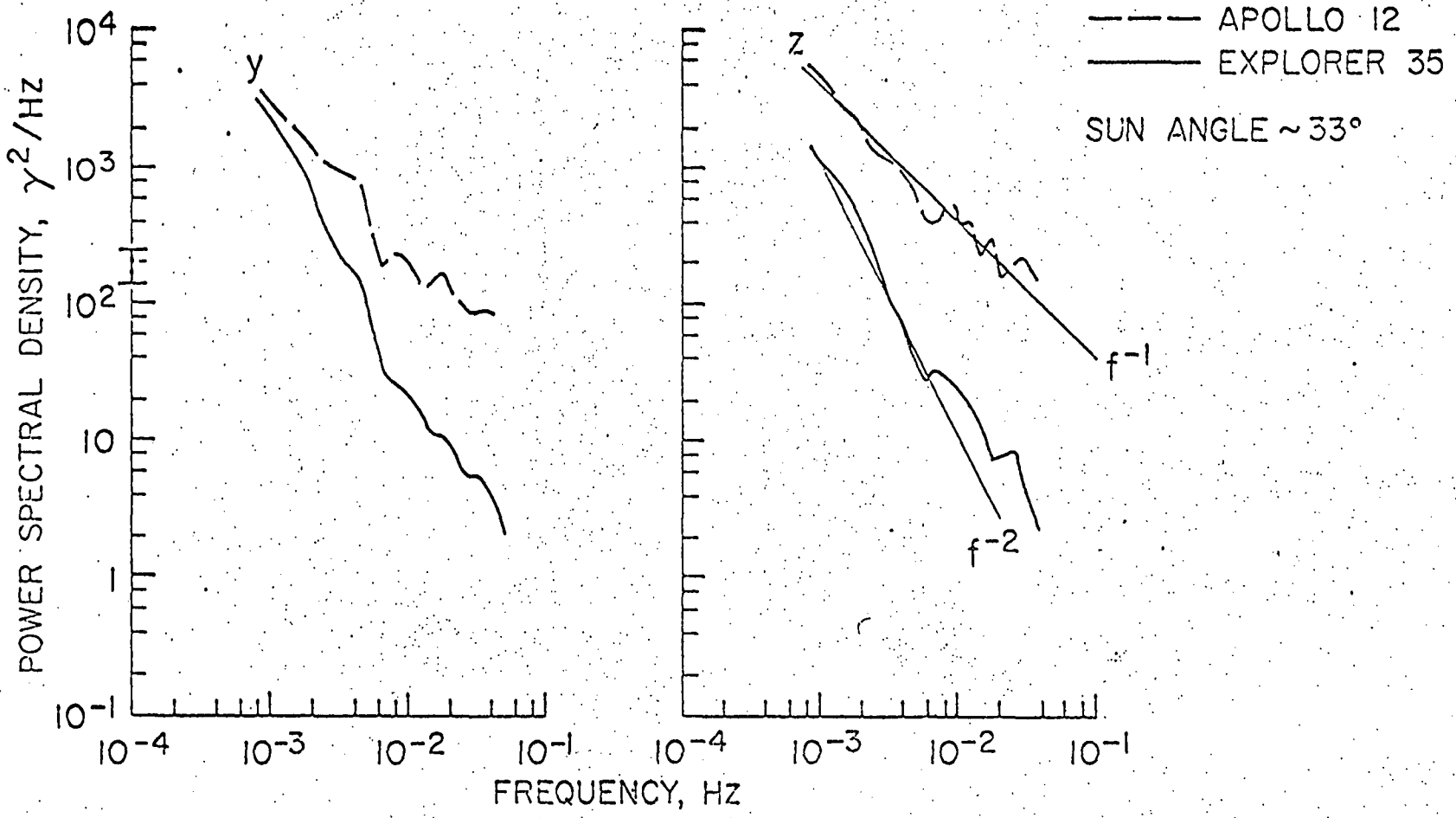
APOLLO 12
EXPLORER 35
SUN ANGLE ~ 33°
y
z
f^{-1}
f^{-2}
POWER SPECTRAL DENSITY, γ^2/HZ
10^4
10^3
10^2
10
1
10^{-1}
10^{-4}
10^{-3}
10^{-2}
10^{-1}
FREQUENCY, HZ

FIGURE 4

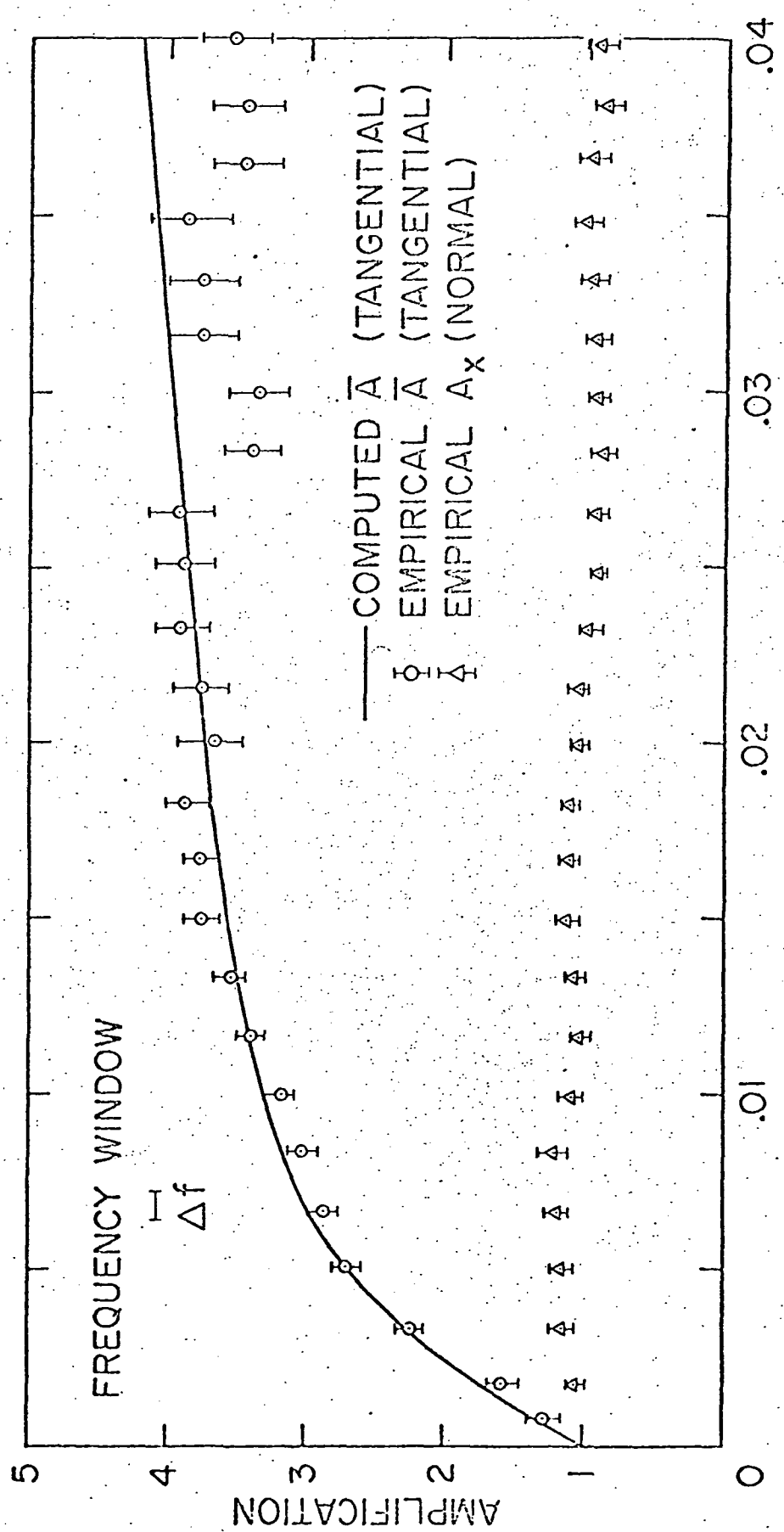
AMPLIFICATION
FREQUENCY, Hz
0
.01
.02
.03
.04
1
2
3
4
5
FREQUENCY WINDOW
Δf
COMPUTED $\overline{A}$ (TANGENTIAL)
EMPIRICAL $\overline{A}$ (TANGENTIAL)
EMPIRICAL A_x (NORMAL)

FIGURE 5

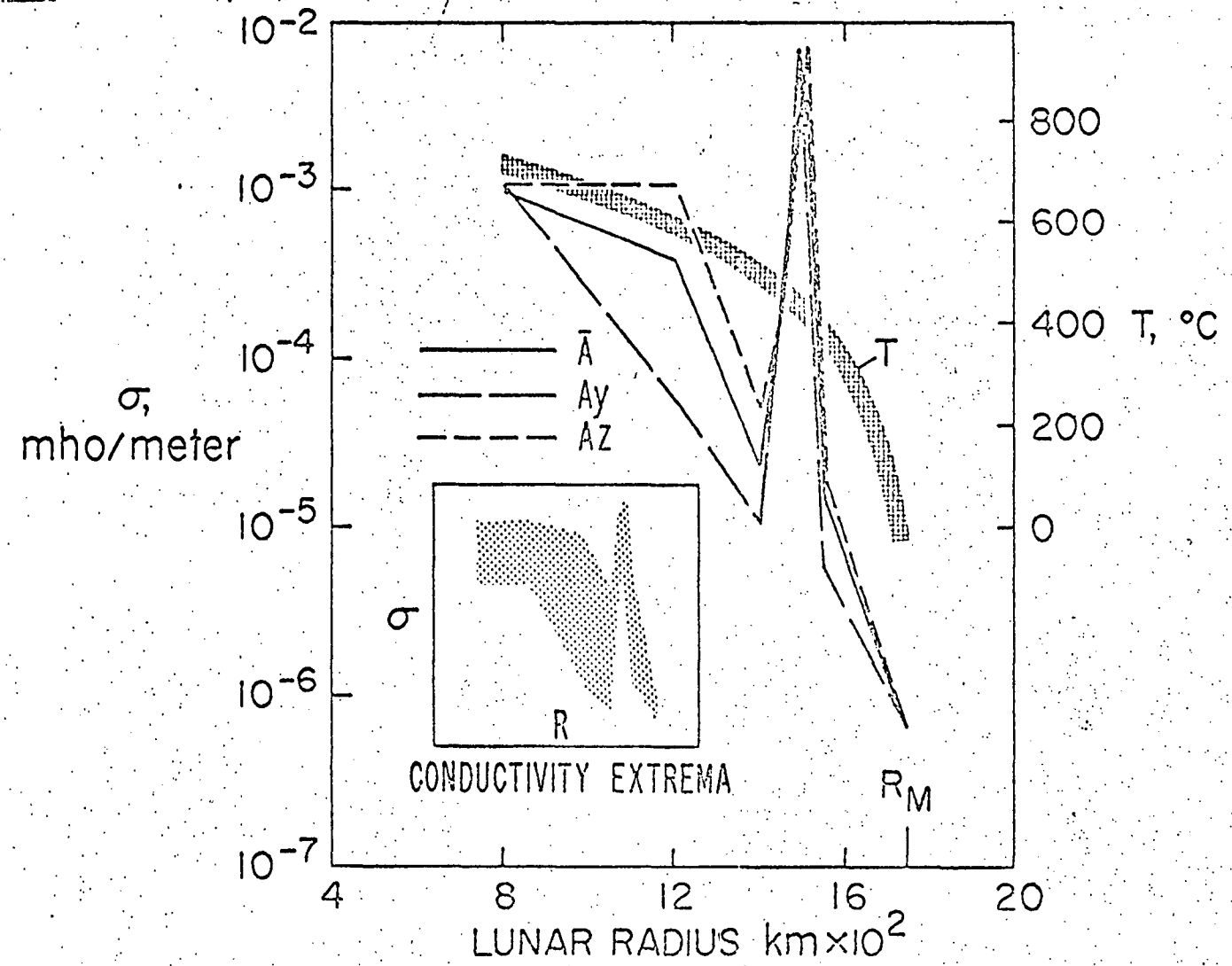
10^{-2}
10^{-3}
10^{-4}
10^{-5}
10^{-6}
10^{-7}
σ, mho/meter
800
600
400 T, °C
200
0
T
Ā
Ay
AZ
σ
R
CONDUCTIVITY EXTREMA
R_M
4
8
12
16
20
LUNAR RADIUS km×10^2

FIGURE 6

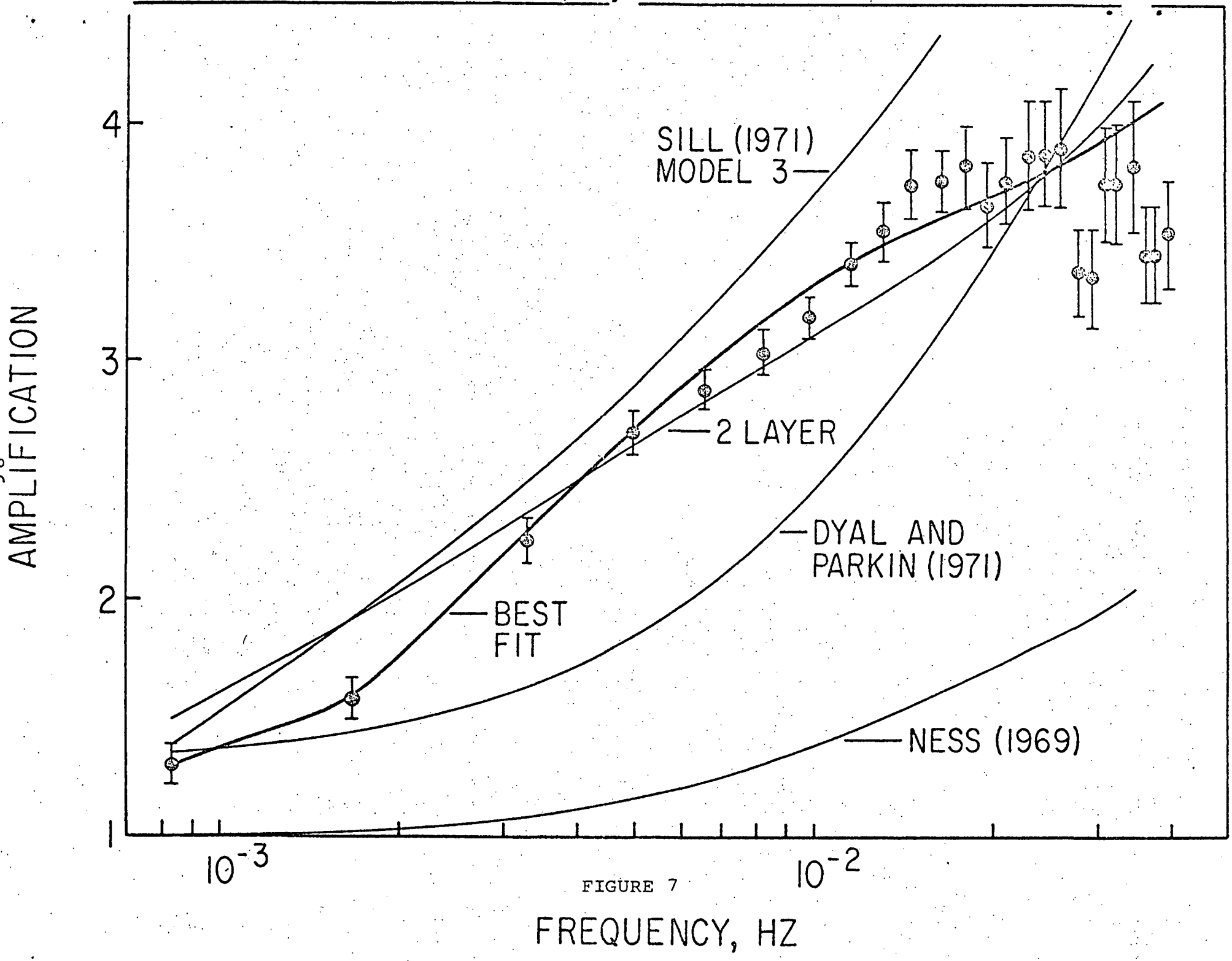
AMPLIFICATION
4
3
2
1
SILL (1971)
MODEL 3
2 LAYER
DYAL AND
PARKIN (1971)
BEST
FIT
NESS (1969)
10^{-3}
10^{-2}
FREQUENCY, HZ

FIGURE 7

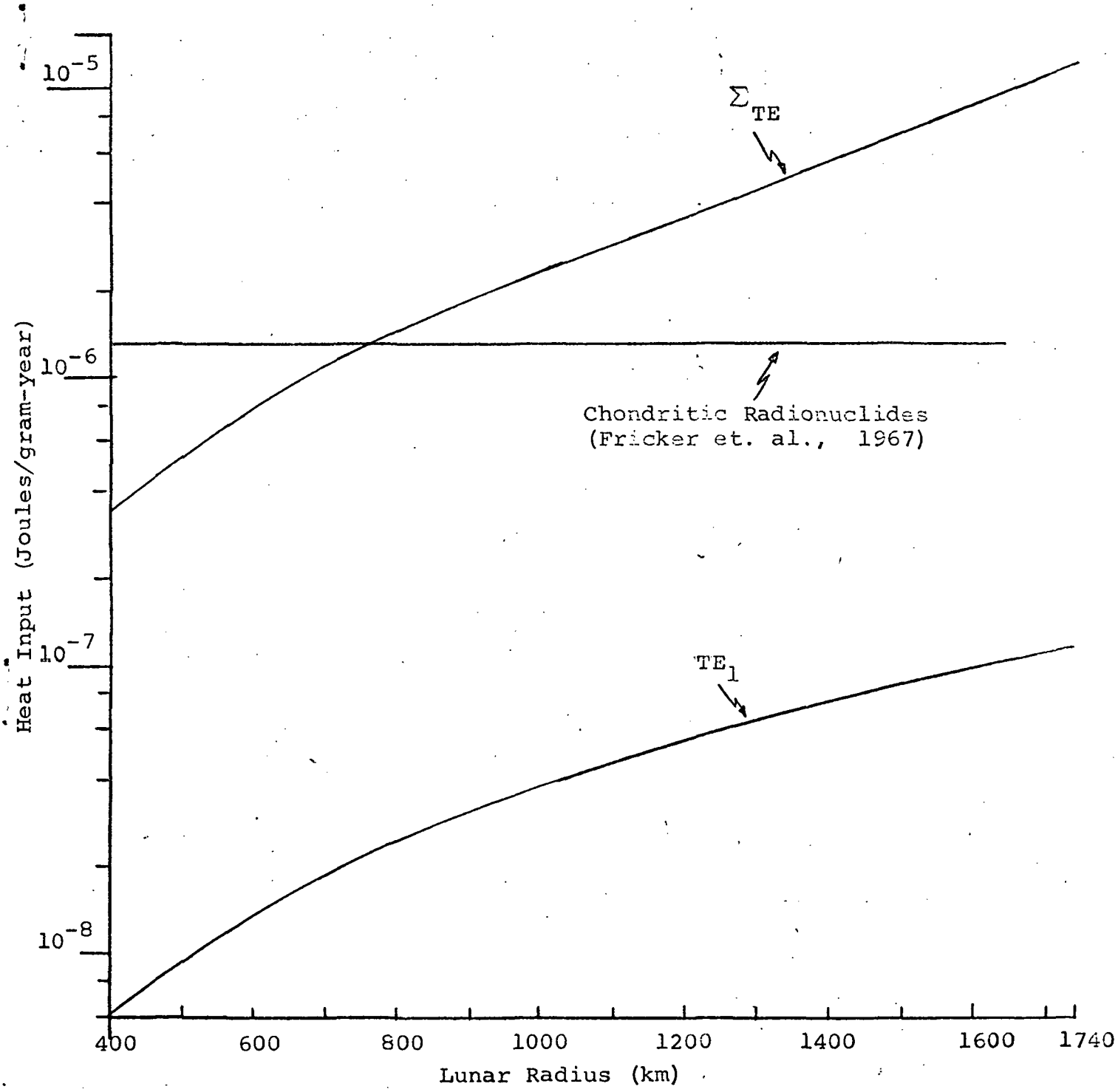
10^{-5}
10^{-6}
10^{-7}
10^{-8}
Heat Input (Joules/gram-year)
Σ_{TE}
Chondritic Radionuclides
(Fricker et. al., 1967)
TE_1
400
600
800
1000
1200
1400
1600
1740
Lunar Radius (km)

FIGURE 8

AMERICAN NUCLEONICS CORPORATION

6036 VARIEL AVENUE, WOODLAND HILLS, CALIFORNIA 91364 PHONE (213) 347-4500